

# Earth and Space Science



## RESEARCH ARTICLE

10.1029/2021EA002034

### Key Points:

- A novel sub-surface ocean detection and characterization method has been developed based on Principal Component Analysis processing of magnetic induction data
- Enables differentiation between ocean-plus-ionosphere and ionosphere-only induction responses in the presence of various noise sources
- Applied here to the compelling target of Triton, thought to possibly harbor a sub-surface ocean beneath a highly conducting ionosphere

### Correspondence to:

C. J. Cochrane,  
[corey.j.cochrane@jpl.nasa.gov](mailto:corey.j.cochrane@jpl.nasa.gov)

### Citation:

Cochrane, C. J., Persinger, R. R., Vance, S. D., Midkiff, E. L., Castillo-Rogez, J., Luspay-Kuti, A., et al. (2022). Single- and multi-pass magnetometric subsurface ocean detection and characterization in icy worlds using Principal Component Analysis (PCA): Application to Triton. *Earth and Space Science*, 9, e2021EA002034. <https://doi.org/10.1029/2021EA002034>

Received 6 OCT 2021

Accepted 11 JAN 2022

### Author Contributions:

**Conceptualization:** C. J. Cochrane, S. D. Vance

**Data curation:** C. J. Cochrane

**Formal analysis:** C. J. Cochrane, R. R. Persinger, S. D. Vance

**Investigation:** S. D. Vance, J. Castillo-Rogez, A. Luspay-Kuti, L. Liuzzo, C. Paty, K. L. Mitchell, L. M. Prockter

**Methodology:** C. J. Cochrane

**Software:** C. J. Cochrane, S. D. Vance

**Validation:** C. J. Cochrane, R. R. Persinger

## Single- and Multi-Pass Magnetometric Subsurface Ocean Detection and Characterization in Icy Worlds Using Principal Component Analysis (PCA): Application to Triton

C. J. Cochrane<sup>1</sup> , R. R. Persinger<sup>2</sup>, S. D. Vance<sup>1</sup> , E. L. Midkiff<sup>1</sup> , J. Castillo-Rogez<sup>1</sup> , A. Luspay-Kuti<sup>3</sup> , L. Liuzzo<sup>4</sup> , C. Paty<sup>5</sup> , K. L. Mitchell<sup>1</sup>, and L. M. Prockter<sup>3</sup>

<sup>1</sup>Jet Propulsion Laboratory, California Institute of Technology, Pasadena, CA, USA, <sup>2</sup>Aerospace Corporation, El Segundo, CA, USA, <sup>3</sup>Johns Hopkins University Applied Physics Laboratory, Laurel, MD, USA, <sup>4</sup>Space Sciences Laboratory, University of California, Berkeley, CA, USA, <sup>5</sup>University of Oregon, Eugene, OR, USA

**Abstract** Many moons in the solar system are thought to potentially harbor hidden oceans based on the features observed at their surfaces. However, the magnetic induction signatures measured in the vicinity of these moons provide the most compelling evidence for the presence of a subsurface ocean, specifically for the Jovian moons Europa and Callisto. Interpretation of these magnetic signatures can be challenging due to the various systematic and random sources of noise that are present in the magnetic field measurement. In this work, a novel magnetometric ocean detection methodology based on Principal Component Analysis is presented and shown to provide enhanced discrimination and geophysical characterization of ocean properties in the presence of noise and error sources. The proposed methodology is robust for a single-encounter mission or an orbiting mission with multiple flybys. Here, it is applied to the Neptunian moon Triton as a prime example of an active, potential ocean world residing in the requisite time-varying magnetic field environment that enables magnetic induction investigation of its interior. In addition to the usual noise sources, other confounding factors are addressed, including the presence of an intense conductive ionosphere, the small amplitude of Neptune's driving magnetic field, and the uncertainty of Neptune's magnetic phase at the time-of-arrival which can potentially hinder accurate ocean detection and characterization. The proposed methodology is applicable to any moon in the solar system residing in a time-varying magnetic field environment.

**Plain Language Summary** The search for habitable oceans in the solar system motivates the need for advances in analytic techniques to positively determine the presence of subsurface oceans in challenging environments. The Principal Component Analysis (PCA) method described in this article is a new paradigm for processing space-based magnetic field measurements for definitive detection and constrained characterization of subsurface oceans. Using Neptune's largest moon Triton as an example ocean world, PCA is directly applied to a three-axis magnetic field data set and shown to be a powerful ocean classification tool for a single or multiple flybys, even in the presence of Triton's highly conducting ionosphere which can mask the magnetic response from the ocean. The method is able to reliably distinguish between the magnetic field signatures associated with the ocean-plus-ionosphere and ionosphere-only model classes and can further determine key characteristics of the hidden ocean in the face of the confounding factors of a conductive ionosphere, local plasma current perturbations, spacecraft timing and position uncertainties, data outages, and various sources of instrument noise. The flexibility and extensibility afforded by the PCA-based method enhance the existing and future capabilities for ocean detection and characterization at candidate ocean worlds throughout the solar system.

## 1. Introduction

Many worlds exist in the solar system with salty subsurface liquid-water oceans beneath icy crusts, facilitated by surface tidal and librational heating. Saturn's moons Enceladus and Titan are known to be water-ocean worlds. Enceladus exhibits impressive jets of water vapor that spray from fissures in the south pole region (Porco et al., 2006), likely the result of tidally driven fault-motion heating of water sourced from a global or regional subsurface ocean below a thick ice shell (Nimmo et al., 2007). Time-varying magnetic induction signatures measured by Galileo's magnetometers in the vicinity of Jupiter's moons Europa and Callisto suggest these bodies also have salty liquid-water oceans beneath their surfaces (Khurana et al., 1998; Kivelson et al., 1999), while

© 2022 Jet Propulsion Laboratory, California Institute of Technology. Government sponsorship acknowledged. This is an open access article under the terms of the [Creative Commons Attribution-NonCommercial License](https://creativecommons.org/licenses/by/4.0/), which permits use, distribution and reproduction in any medium, provided the original work is properly cited and is not used for commercial purposes.

**Visualization:** C. J. Cochrane  
**Writing – original draft:** C. J. Cochrane, R. R. Persinger, E. L. Midkiff  
**Writing – review & editing:** C. J. Cochrane, R. R. Persinger, S. D. Vance, E. L. Midkiff, J. Castillo-Rogez, L. Liuzzo, C. Paty, K. L. Mitchell, L. M. Prockter

recent Hubble investigations indicate a large underground water ocean at Ganymede (Saur et al., 2015). Although limited data exists, many moons of the gas giants are thought to possibly contain hidden oceans. The five large Uranian moons (Miranda, Ariel, Umbriel, Titania, and Oberon) all in some form exhibit surface features consistent with a subsurface liquid ocean (e.g., Croft & Soderblom, 1991; Schenk et al., 2020), and also reside in a time-varying magnetic environment which enables magnetic induction detection (Arridge & Eggington, 2021; Cochrane et al., 2021; Weiss et al., 2021). Neptune's moon Triton, the focus of this article, is a particularly compelling mission target with numerous characteristics consistent with the presence of a subsurface ocean. Tidal heating from a highly inclined retrograde orbit, evidence of cryovolcanic activity, active plumes, (Kirk et al., 1995), and unusual geological features (Ivanov et al., 1991) imaged by Voyager 2 suggest the possibility of a liquid layer beneath the surface (Croft et al., 1995; Nimmo & Pappalardo, 2016). The Outer Planets Assessment Group Roadmap to Ocean Worlds (Hendrix et al., 2019) states that “*Triton is the highest priority ocean world ... to target in the near term.*”

Spacecraft equipped with a 3-axis magnetometer have been able to confirm that some of these moons are indeed ocean worlds based on the magnetic induction signatures measured near their surfaces, Europa and Callisto being the prime examples. In this work, a novel ocean detection methodology based on Principal Component Analysis (PCA) is used to directly process the magnetic induction fields measured by a magnetometer, significantly increasing positive discrimination and geophysical characterization of a subsurface ocean in the presence of various noise and magnetic error sources. The proposed methodology is shown to be robust for a single-pass encounter or a multi-pass orbiting mission at a variety of other possible ocean worlds including the moons of Uranus or Jupiter, each with a unique magnetospheric environment. In this work, the following key concepts are presented: ocean induced magnetic moments (MMs), scaled induced magnetic moments (SMMs), magnetic separation (MS) of *ocean* and *no-ocean* classes, and the influence of the spacecraft trajectory through a moon's induction fields. Also presented is the method's sensitivity to instrument parameters (sample-rate, noise, and offsets), spacecraft uncertainties (position, attitude, and timing), and anticipated plasma currents. Prior to presenting PCA's applicability to ocean detection and characterization, an independent closed form analytical verification of the methodology based on discrete-time signal energy preservation of the magnetic field time-series is described. Finally, PCA's transformation of the high-dimensional magnetic field time-series into a reduced, visually convenient, 3-dimensional SMM ocean classification space and the resulting ability to clearly distinguish the presence of a conductive liquid layer are illustrated.

## 2. Subsurface Ocean Detection Using Magnetometric Data

### 2.1. The Favorable Magnetic Environment at Triton

The phenomenon of magnetic induction occurs when a time-varying magnetic field induces electrical eddy currents within a conducting medium such as a subsurface salty ocean, which in turn generates a secondary induced magnetic field that can be remotely sensed by a magnetometer. Neptune's largest moon Triton represents a potential ocean world of high interest to the science community (Hansen et al., 2021; Hendrix et al., 2019). It is immersed in Neptune's strong time-varying magnetic field, which facilitates magnetic induction investigation of its interior.

Neptune's unusual magnetic field has a large MM ( $13,300 \text{ nT-R}_N^3$  or  $2.2 \times 10^{17} \text{ T-m}^3$ , roughly 27 times that of Earth's), with a magnetic pole tilted  $47^\circ$  with respect to Neptune's spin axis and shifted by  $0.55 R_N$  from Neptune's center (Connerney et al., 1991). The spin axis is tilted  $28^\circ$  with respect to the normal of the ecliptic plane, and Triton's retrograde orbit is a steeply inclined  $157^\circ$  relative to Neptune's equator. As a result of this complicated geometry, Triton experiences cyclic variations in Neptune's driving field at two fundamental periods: the synodic period of Neptune's rotation ( $\sim 14 \text{ hr}$ ) and Triton's own orbital period ( $\sim 141 \text{ hr}$ ; Saur et al., 2010). Harmonics and beat frequencies between these two fundamental periods are lower in amplitude but still provide measurable ( $>1 \text{ nT}$ ) contributions to the total external driving fields.

The periodic variation in the magnetic field at Triton as it cyclically traverses Neptune's magnetic latitudes critically enables magnetometric ocean detection. A fortuitous additional advantage of this orbital configuration is that Triton spends minimal time within a couple of planetary radii ( $<2 R_N$ ) of Neptune's magnetic equator, where plasma effects are anticipated to be at their largest and roughly confined to a sheet that corotates with the planet (Mejnertsen et al., 2016). Moreover, when Triton does interact with the plasma sheet, particle densities are

expected to be very low at Triton's significant distance from Neptune ( $14 R_N$ ), measured at  $0.003/\text{cm}^3$  by Voyager 2 (Zhang et al., 1991) As a result, induced fields from plasma currents minimally perturb the local magnetic field around Triton (Liuzzo et al., 2021).

However, the surprisingly intense ionosphere of Triton presents a potential confounding factor, because induced electrical currents in the ionosphere generate a secondary magnetic field which could mask an induction response originating from an ocean (Hartkorn & Saur, 2017). Radio occultation measurements made by Voyager 2 found peak electron concentrations of  $2.3\text{--}4.6 \times 10^4 \text{ cm}^{-3}$  (Tyler et al., 1989). This signal is significantly higher than can be attributed to solar UV, which suggests precipitation of charged particles from Neptune's magnetosphere (Ip, 1990; Mandt, 2019; Sittler & Hartle, 1996; Strobel, 1990; Yung & Lyons, 1990). Another concern is that at Triton's orbital distance, the strength of Neptune's driving field is reduced to levels well below those encountered at the Jovian moons, complicating ocean detection when accounting for potential sources of measurement error and systemic noise. Additionally, because of Neptune's gaseous outer layer, its core rotation period—and therefore the phase of the synodic (14 hr) magnetic wave—will remain unknown until arrival at the Neptune system. An ocean detection method for a single flyby of Triton must be able to distinguish between ocean and ionosphere induction signals for any magnetic phase of the synodic period.

## 2.2. New Approach for Subsurface Detection

The conventional approach to detecting a conductive subsurface ocean is least squares inversion of the magnetic induction field time-series measured by a magnetometer, making use of the spacecraft's trajectory and the dipole field equation (see Kivelson et al., 2002 and Schilling et al., 2004 for related inversion schemes). For a single flyby of a particular moon, a data inversion step can be used on the three-channel magnetometer data to yield the three-element total induced MM vector generated from the subsurface ocean at closest approach. This induced MM is formed from the sum of the individual MMs associated with the ocean's response to the two primary waves (synodic and orbital), including the associated harmonics and beat frequencies of the two fundamental periods, and provides insight into the properties of the ocean.

The novel approach described in this article first formulates a large data set of forward-modeled induced dipole magnetic field time-series, generated from thousands of different potential interior models, and then processes this data using the well-established data-dimensionality reduction technique of PCA. Noisy magnetic field measurements acquired near the body of interest can then also be broken down into their principal components (PCs) to distinguish between *ionosphere-only* and *ocean-plus-ionosphere* model classes. This method uses all available information in the processing (i.e., nothing is discarded) and the retained signal energy increases the separation between model classes. At bodies like Triton where the strength of the driving magnetic field, and hence the induced fields, are relatively small, this boost in separation reduces false positive and false negative ocean classifications of noisy measurements.

## 2.3. Two Distinct Methodology Pathways

Subsurface ocean detection is enabled by 3-axis magnetometer measurements acquired in the vicinity of a planetary body immersed in a time-varying magnetic field. In any realistic scenario, relatively close proximity to the body's surface is necessary to achieve useable measurements because field strength falls off rapidly with distance from the center of the moon (e.g.,  $1/r^3$  for a dipole response and  $1/r^4$  for a quadrupole response). Figure 1 (left) illustrates the magnetic field lines associated with sum total of Neptune's magnetospheric field and the induction field at Triton, color-coded according to field strength in units of nanoteslas (nT), along with an example single-pass trajectory (white line). The data measurement interval of interest for a single flyby (velocity  $\sim 18 \text{ km/s}$ ) spans roughly  $\pm 6 \text{ min}$  about closest approach to Triton, at a minimum altitude above the surface ( $R_T = 1,353.4 \text{ km}$ ) of less than  $400 \text{ km}$  ( $r = 1,754 \text{ km}$ ).

To reliably ascribe the measured induced response from the combination of a conducting subsurface ocean and conducting ionosphere, an extensive set of induced magnetic field time-series is forward modeled for a wide range of plausible physical properties of Triton's known ionosphere and its potential ocean as described in Section 3.2. To cover this range of possibilities, a parameter space of more than 13,000 combinations of ocean and ionosphere characteristics is defined for this study, and the magnetic responses are computed per a multi-shell conductivity model, described in more detail in Section 3.2. Figure 1 (right) depicts the anticipated measured total magnetic

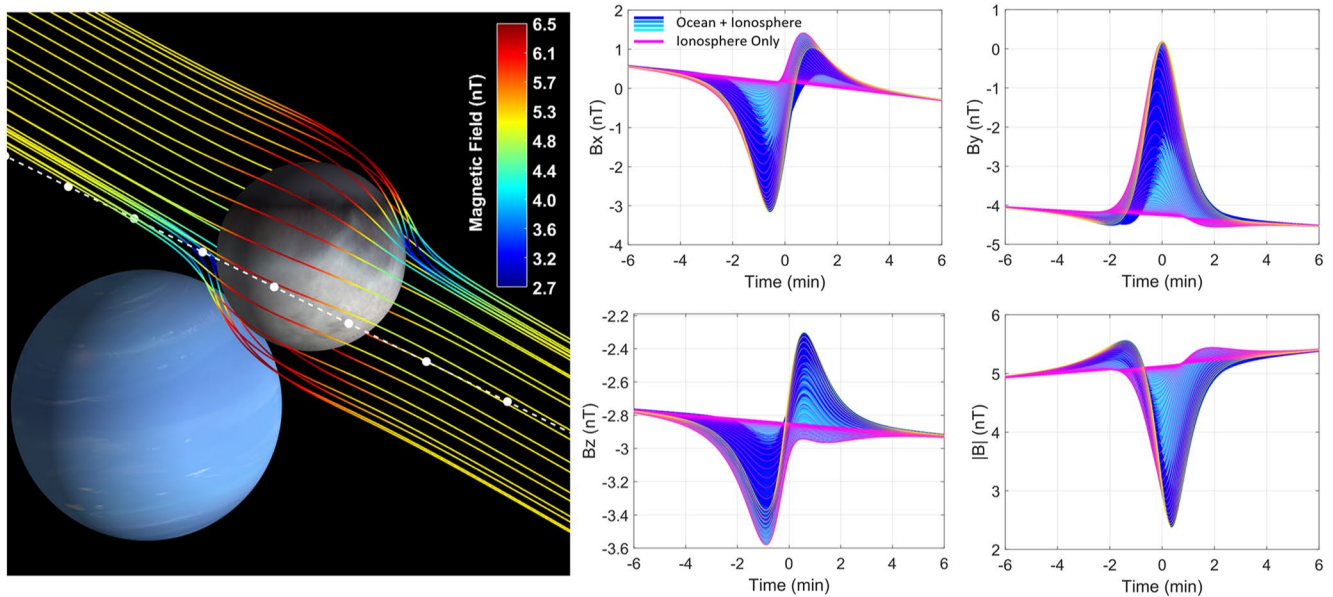


**Figure 1.** The approach described uses forward modeling of magnetic response functions resulting from Neptune's magnetic field interacting with a wide range of plausible ionosphere and ocean properties. (left) Simulated magnetic field lines of the total magnetic field in the vicinity of Triton including Triton's induced magnetic field and Neptune's magnetic field at a time near the closest approach of the moon. The white dashed line with white dots illustrates the nominal flyby trajectory used for this analysis. (right) Forward modeled magnetic field time-series evaluated along the flyby, blue indicative of ocean plus ionosphere responses and magenta of ionosphere-only responses.

field over the 12-min encounter period. The simulated magnetometer signals colored in magenta represent the ionosphere-only models, and the ocean-plus-ionosphere models are represented by shades of blue. From the figure, it is obvious that the difference between the ionosphere-only (magenta) and ionosphere-plus-ocean (blue shades) model time-series is difficult to differentiate based on line shape and amplitude alone. This suggests the need for more powerful data analysis tools.

Figure 2 depicts two possible paths for ocean detection; Path 1 illustrates the traditional data inversion technique with an additional stage of MM forward modeling and Path 2 illustrates the PCA methodology. Both paths depend on forward modeling the total induced MMs for various interior magnetic induction models, which depend on the ocean and ionosphere parameter space and the driving magnetic field (15 individual magnetic waves with different frequencies were simulated) of the parent planet as described in Section 3.1. The time-varying portion of the total induced MM, evaluated at closest approach, for each model is a 3-element vector  $[M_x, M_y, M_z]$  (see Section 3.4). Only  $M_x$  and  $M_y$  of all models are plotted in the figure, as they contain the most information. Ocean-plus-ionosphere (blue shades) and ionosphere-only (magenta) models are distinguished by color. It is precisely these computed quantities that serve as the MM classification space for the data inversion methodology taken in Path 1. Using the spacecraft trajectory ephemeris and the magnetic dipole field equation, Path 1 entails inverting the magnetic field measurements to obtain a representative MM that can be projected into the ocean classification space (represented by orange dot in the figure) for ocean property inference. The separation from the magenta ionosphere-only models (in units of nT) is a representation of ocean detection confidence.

Path 2 also requires the use of the forward modeled induced MMs but uses them to compute the induced dipole magnetic field time-series along the spacecraft trajectory for all ionosphere-only and ocean-plus-ionosphere models. These induced magnetic field time-series are represented by  $3N$  samples ( $N$  samples for each of the three channels of the magnetometer, dictated by the sampling rate) and are directly fed into the PCA data analysis tool for dimensionality reduction (further described in Section 5). The PCs of all models that are computed in this path are defined by a 3-element vector  $[PC1, PC2, PC3]$ , and can also be used as an ocean classification space (only PC1 and PC2 are shown in the block diagram). In this process, PCA computes a set of eigenvectors that are used to project the measurement (also a total of  $3N$  samples in length) into the PCA ocean classification space, again represented by the orange circle. With both classification spaces characterized by units of nT, note the larger separation between the two model classes (blue and magenta) for the PCA ocean classification space.

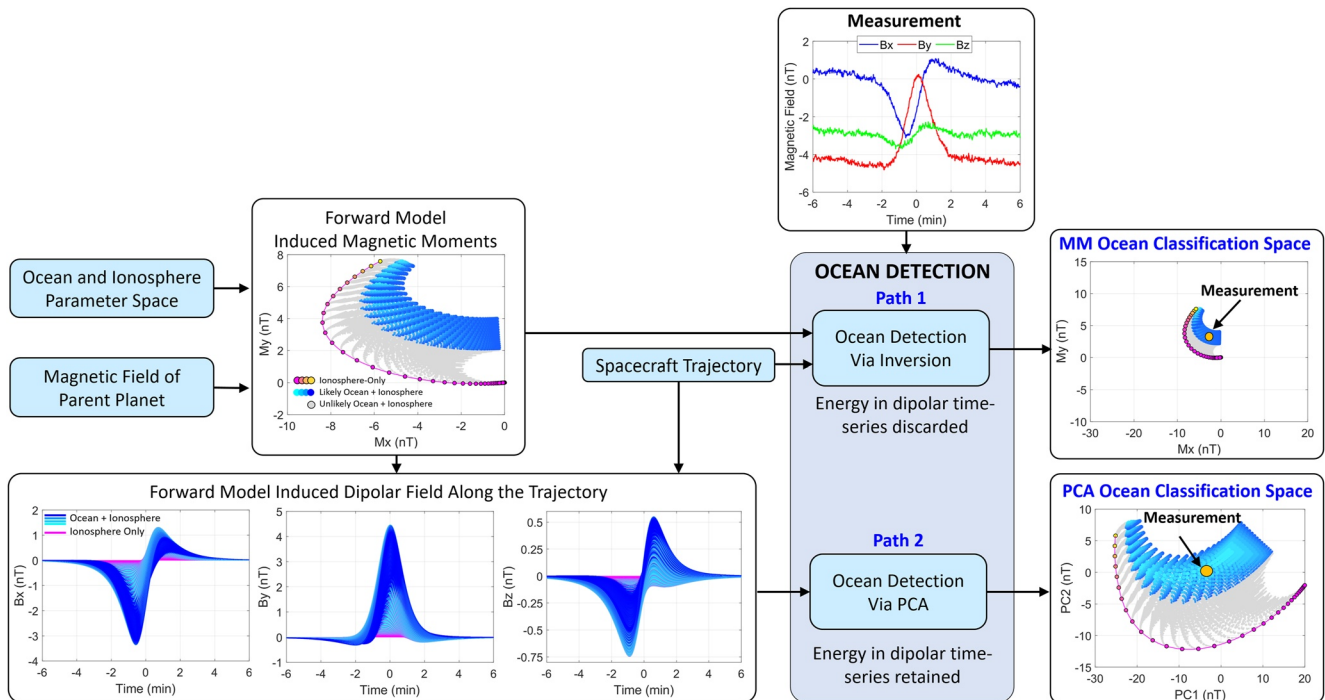


**Figure 2.** Block diagram illustrating the high-level steps that need to be performed for ocean detection using single inversion/least squares (Path 1) and the novel PCA scheme described in this article (Path 2). Some current ocean detection approaches extend Path 1 and perform a second stage of inversion to recover individual magnetic moments for select magnetic waves of interest. Both paths provide the ability to perform ocean detection; however, the PCA path results in larger separation between the two model classes.

While PCA has been widely used for decades in a variety of data analysis applications to reveal correlations in multi-dimensional experimental data, its novel application to magnetometer measurements for ocean detection demonstrates a significant advantage by reducing the time-dimensionality of the induced dipolar magnetic field time-series into a more easily visualized 3-dimensional space in which separation between ocean-plus-ionosphere and ionosphere-only data classes is systematically increased. Because PCA is applied directly to the magnetic field time-series acquired by the magnetometer, the computed PCs retain all signal energy owing to the orthonormality property of the eigenvectors used for the linear projection. The PCs of the models effectively represent the superposition of SMMs. This scaling provides increased separation (relative to the MM classification space) between the two different model classes and is a direct result of the physical relationship between the dipolar fields and the MMs that generate them (see Sections 3.4 and 3.5).

As the information about a moon's interior (ocean depth, thickness, and conductivity) is contained within the induced MMs, both ocean detection methodology paths are generally viable based on the separability of the distinctive data models that contain oceans and ones that do not. However, for ocean detection at Triton—and for investigations of other candidate ocean worlds—ocean detection using PCA is advantageous because the *scaled total MMs* increase the MS between the ionosphere-only and ionosphere-plus-ocean model classes enhancing distinguishability for ocean detection purposes. By contrast, inverting for the total MMs discards signal energy, resulting in a comparatively reduced MS between data classes.

### 3. Forward Modeling the Induced MMs and Dipole Response

#### 3.1. Neptune's Magnetic Field and Plasma Sheet Geometry

Measurements made by *Voyager 2* in the magnetosphere of Neptune revealed that Triton resides in a highly dynamic magnetic field environment, ideal for magnetic induction investigation into the presence of a subsurface ocean. Neptune's magnetic field likely originates from a self-sustaining dynamo acting within a thin electrically conductive and convective shell (Hubbard et al., 1995; Podolak et al., 1995; Ruzmaikin & Starchenko, 1991; Soderlund & Stanley, 2020; Stanley & Bloxham, 2004; Stanley & Bloxham, 2006). The magnetic field model

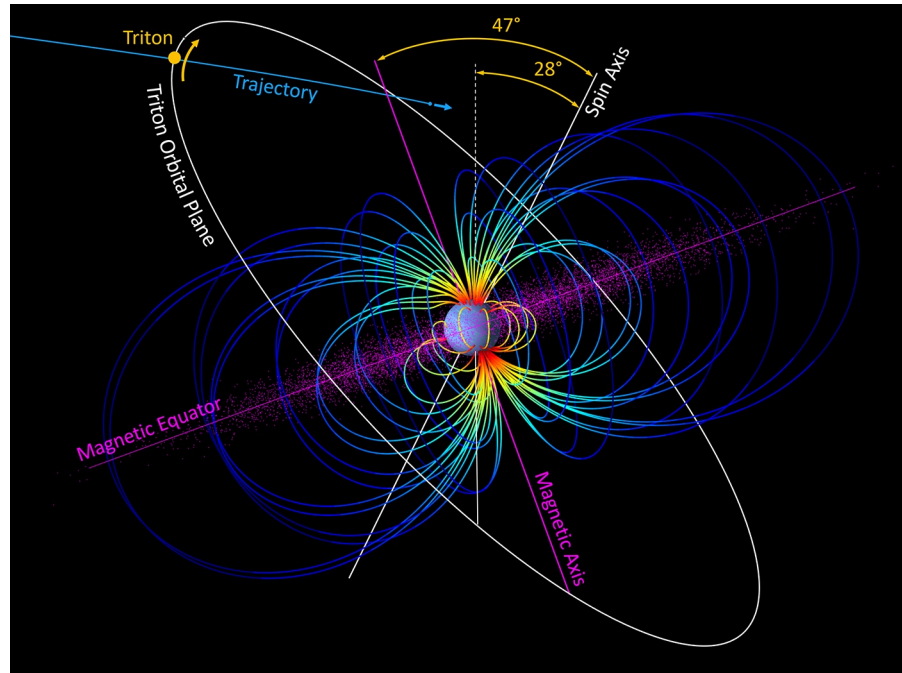


**Figure 3.** Geometrical representation of the Neptune system, illustrating the tilt of Neptune's spin axis, the tilt of Neptune's magnetic axis with respect to its spin axis, the orbit of Triton, the magnetic equator populated with corotating plasma particles, and the baseline trajectory of the spacecraft used in this work.

developed from the *Voyager 2* data (Connerney et al., 1991) is described by the negative gradient of the scalar potential,  $\mathbf{B}_N = -\nabla V$ . The spherical harmonic expansion of the scalar potential is expressed as:

$$V = R_N \sum_{n=1}^N \left( \frac{R_N}{r} \right)^{n+1} \sum_{m=0}^n \{ P_n^m(\cos\theta) [g_n^m \cos(m\phi) + h_n^m \sin(m\phi)] \}, \quad (1)$$

where  $R_N$  is the equatorial radius of Neptune;  $r$  is the radial distance to the center of the planet;  $\theta$  is the colatitude;  $\phi$  is the longitude;  $P_n^m(\cos\theta)$  are the Schmidt-normalized Legendre functions of degree  $n$  and order  $m$ ; and  $g_n^m$ ,  $h_n^m$  are the internal Schmidt coefficients.

Figure 3 illustrates the magnetic field lines and magnitudes associated with this model, including the large tilt ( $47^\circ$ ) of Neptune's magnetic axis with respect to its spin axis (which is tilted  $28^\circ$  respect to the normal of the orbital plane), and the highly inclined tilt of Triton's orbit. Evaluating the field model at the position of Triton reveals that the moon experiences variations in the field at Triton's orbital period ( $T_{\text{orbit}} = 141$  hr) due to its orbital inclination and also experiences variations in the magnetic field due to Neptune's rotation. As Neptune rotates every  $T_{\text{spin}} = 16.1$  hr, the apparent rotation period of the planet observed from Triton (i.e., the synodic period) is defined by  $T_{\text{synodic}} = 1/(1/T_{\text{spin}} + 1/T_{\text{orbit}})$ , roughly every 14.5 hr. Note that the synodic period is shorter than Neptune's rotation period due to Triton's retrograde orbit.

The left panel of Figure 4 illustrates the magnetic field time-series of Neptune evaluated at the position of Triton, and the top right panel of the figure represents the associated frequency spectrum. In the Triton reference frame, the  $z$  axis is aligned with Triton's spin axis, the  $x$  axis is in the direction of Neptune, and the  $y$  axis completes the right-handed orthogonal system, roughly in the direction of the moon's orbital motion. Aside from the presence of the two dominant variations of the magnetic field that occur at the prime frequencies, the 14-hr synodic period and the 141-hr orbital period, there are also variations that occur at the beats and harmonics of these two fundamental periods. This AC portion of the magnetic field time-series of Neptune  $\mathbf{B}_N$  at Triton can be modeled by a linear superposition of sinusoids:

$$\mathbf{B}_N(t) = \sum_k \mathbf{B}_{N,k}(t) = \sum_k \mathbf{B}_k e^{i(2\pi f_k t + \theta_k)}, \quad (2)$$

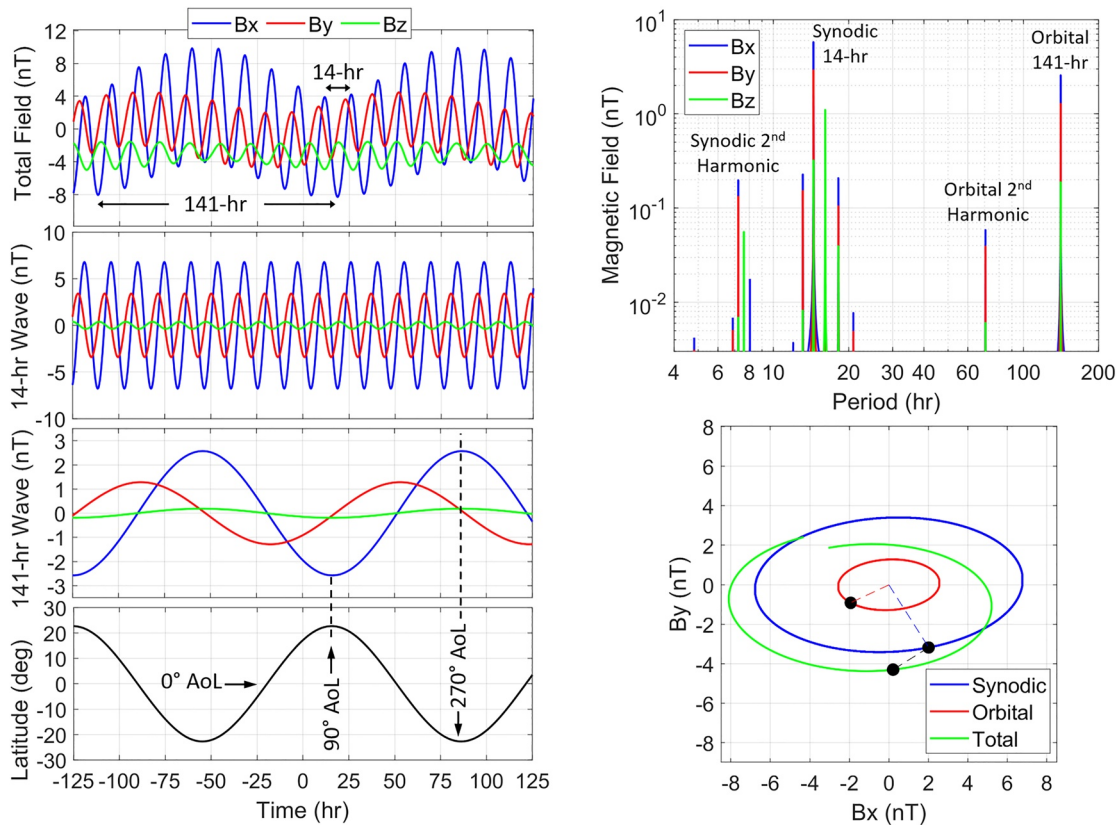


**Figure 4.** The combination of Neptune's tilted spin axis and Triton's inclined orbit causes the magnetic field to vary at multiple frequencies in Triton's fixed frame, dominated by Neptune's 14-hr synodic period and Triton's 141-hr orbital period. This is important in the context that the interaction path length is greater for longer period magnetic waves, thus the 141-hr period wave more readily penetrates conductive layers, including Triton's ionosphere. (left panel) From top-to-bottom, the total magnetic field time-series evaluated at the orbit of Triton, the 14-hr synodic magnetic field time-series components, the 141-hr magnetic field time-series components, and Triton's latitudinal position in Neptune's geographic frame. (top right) Magnetic field spectrum of the time-series illustrated in the top left plot. (bottom right) Hodograph comparing the  $B_x$  and  $B_y$  components (in IAU Triton frame) of Neptune's synodic, orbital, and total magnetic waves observed in the Triton reference frame. The total wave in this image only spans about  $\pm 7$  hr with respect to closest approach, where the time of closest approach is indicated by the black dots along each curve.

where  $\mathbf{B}_{N,k}(t)$  is the  $k$ th discrete magnetic wave of Neptune at frequency  $f_k$ ,  $\mathbf{B}_k = [B_{x,k} \ B_{y,k} \ B_{z,k}]$  are their amplitudes and  $\boldsymbol{\theta}_k = [\theta_{x,k} \ \theta_{y,k} \ \theta_{z,k}]$  are their phases (referenced with respect to the J2000 epoch in this work). The individual waves with the 15 largest amplitudes are used for analysis as illustrated in the top right of Figure 4 (see Table A1 in the Appendix for a complete table of magnitudes and phases for each of these waves, solved using a least squares inversion approach on the magnetic-field time-series). Note that the strength of the orbital wave ( $B_x = 2.6$  nT) is the same order of magnitude of the synodic wave ( $B_x = 6.8$  nT), which can cause the total MMs to add constructively or destructively in a significant fashion (see Section 6.2). This coincidence is not encountered at any other potential ocean world in the solar system, making Triton an ideal body for multi-frequency magnetic induction investigation.

Also plotted in the left panel of Figure 4 along with the total magnetic field time-series are depictions of the time-series broken down into the individual synodic and orbital periods. The phase of the synodic field illustrated is based on the Connerney et al. (1991) magnetic field model of Neptune (referenced in this work as  $0^\circ$  magnetic phase) but will be unknown until future spacecraft arrival. The magnetic phase is unknown because the rotation of Neptune's core is not visible from Earth and no spacecraft have visited the Neptune system since Voyager 2 in 1989. Furthermore, remote observations of aurora at Neptune, which could help to identify and constrain the location of the magnetic poles, remains elusive (Lamy, 2020). Note that the orbital or 141-hr magnetic wave field strength is maximized when Triton is at the highest Neptune latitude ( $\pm 23^\circ$ ), corresponding to an orbital argument of latitude (AoL) of  $90^\circ$  and  $270^\circ$ . Because Triton's orbit is almost perfectly circular, variations in the magnetic field are not attributable to changes in distance with respect to Neptune, but rather are due to changes

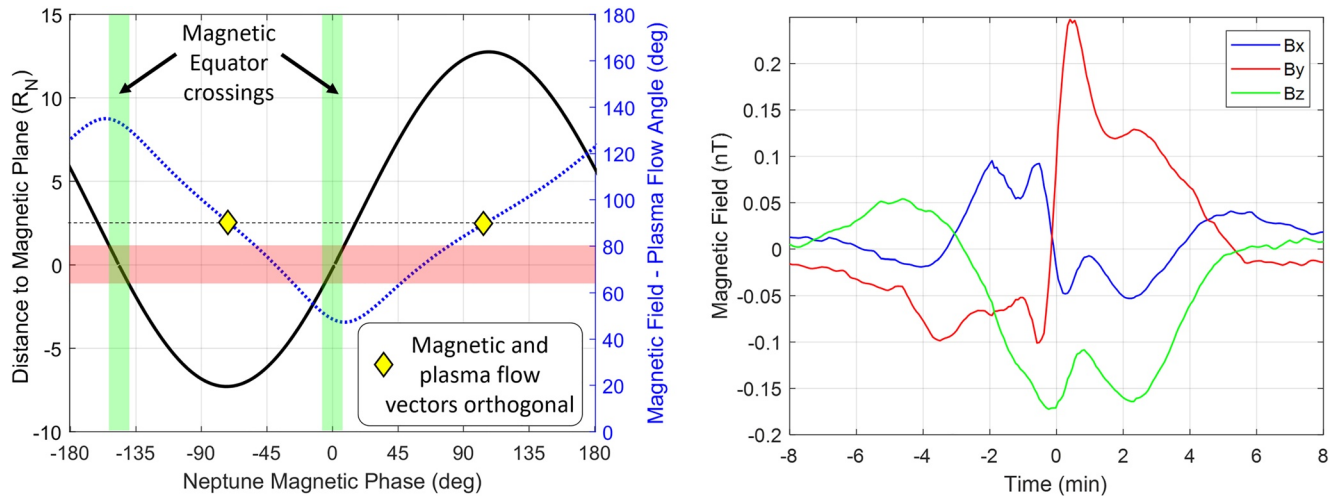


**Figure 5.** Interference from the plasma interaction is not anticipated to be significant for ocean detection at Triton. (left) Triton's distance from Neptune's magnetic equator (black solid line) and the magnetic field—plasma flow angle (dotted blue line) are shown as a function of Neptune magnetic phase at the 14-hr synodic period. The red bar indicates a range  $\pm R_N$  about the magnetic equator, representing a region where plasma currents are anticipated to be at their strongest. (right) Hybrid modeling indicates that plasma interaction fields (isolated from the induced dipole response of Triton) along the baseline trajectory resulting from the plasma currents in Neptune's magnetosphere are of minimal magnitude (corresponding to  $0^\circ$  magnetic phase and  $50^\circ$  argument of latitude).

in position with respect to Neptune's magnetic latitude because the field is two times stronger at the poles of the dipole than at the magnetic equator.

In addition to Triton's ionosphere induction response, Triton's magnetic environment is also affected by the moon's interaction with the magnetospheric plasma. The density of the ambient plasma fluctuates by nearly an order of magnitude as Neptune's magnetic equator and plasma sheet sweep over Triton. As a result, the interaction between the magnetospheric plasma, Triton's atmosphere/ionosphere, and the induced field is time-variable. As shown in Figure 5 (left), Triton spends the majority of its orbit far from Neptune's magnetic equator, in regions where the magnetic field perturbations associated with Triton's plasma interaction are negligible compared to the strength of the induced field. During the short intervals when Triton traverses Neptune's magnetic equator (coincidentally corresponding to a time associated with the baseline trajectory used in this work), results of hybrid modeling (Müller et al., 2011) by Liuzzo et al. (2021) indicate that the magnitude of plasma interaction fields will be minimal with perturbations below 10% of the background field (see Figure 5 right), even when conservatively assuming a plasma density an order of magnitude higher than measured by Voyager 2.

Moreover, the flow direction of  $47^\circ$  with respect to the background field is more favorable than the  $90^\circ$  cases that fortuitously occur when the center of the plasma sheet is more than  $3 R_N$  distant. The  $47^\circ$  or  $133^\circ$  flow direction reduces the perturbing effects that plasma interaction fields could have on the induced magnetic field originating from a subsurface ocean. Moons in the Jovian system commonly experience strong plasma interaction effects due to the high density of particles in the current sheet and orthogonal orientation of Jupiter's field with respect to this current system (e.g., Liuzzo et al., 2016, 2017, 2018). Triton not only experiences much weaker plasma density (and associated currents), but its highly inclined orbit and Neptune's magnetic rotational geometry further reduce the perturbing effects of the plasma interaction to the point where it can be simply treated as a systematic noise source for ocean detection purposes.

### 3.2. Ocean and Ionosphere Parameter Space Definition

Inclusion of a wide range of ocean, ionosphere and ice-shell characteristics that could realistically be encountered at Triton is a key element of the ocean detection forward modeling process, for both pathways in Figure 2. A set of 13,056 potential ocean and ionosphere models is defined, and for each model the induced dipolar field that could be potentially detected is derived. Analysis of Voyager 2 data (Strobel et al., 1990) found a best-fit for the ionosphere conductance in the range of 10,000–20,000 Siemens (S), but based on expected local magnetic field variations at Triton, the range could likely extend to 4,000–36,000 S. Considering the potential for increased

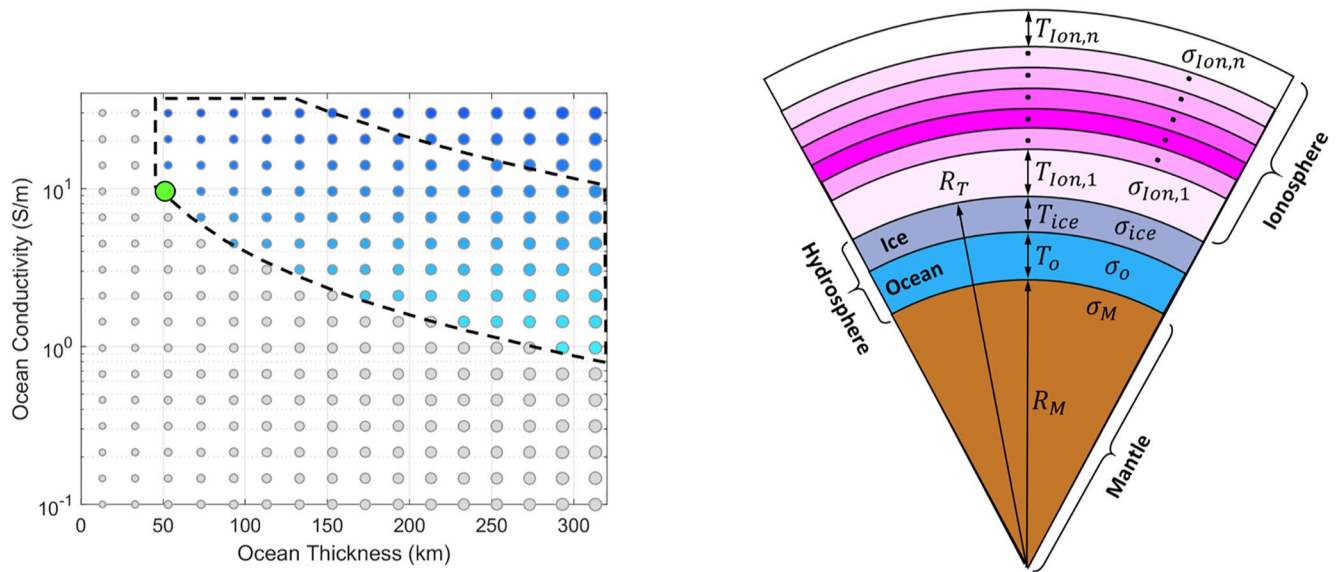


**Figure 6.** This analysis is informed by a deep exploration of a wide range of possible ocean and ionosphere parameters. (left) The 256 modeled oceans comprising the ocean parameter space used to forward model the various complex response functions associated with Triton; the size of the circles indicates relative ocean thickness (smaller circles represent thinner, and therefore deeper oceans for a given hydrosphere thickness), while the circles' color represents relative ocean conductivity. The models contained within the black dashed contour represent the members of the ocean parameter space that are geophysically most likely, with the green circle representing the case within this subset that is most difficult to detect (an ocean with a thickness of 50 km and 9 S/m conductivity). This ocean is referred to as the least-favorable likely ocean throughout this manuscript. Note that because salt mass is conserved in aqueous solution, thinner oceans are typically associated with higher conductivities, themselves a function of salt concentration. (right) The multi-shell model of Triton entails a non-conductive rocky mantle, a conductive ocean of thickness  $T_o$ , a non-conductive ice shell of thickness  $T_{ice}$ , and conductive ionosphere which can be modeled with an arbitrary number of conductive layers  $n$  of varying conductivity  $\sigma_{ion}$  and thickness  $T_{ion}$ .

electron concentrations and electron temperatures, and to add margin, 51 ionosphere conductance values ranging from 0 to 100,000 S were considered for this analysis.

For this analysis, 256 ocean models are defined which, combined with 51 ionosphere models, yield 13,056 model cases comprising the overall ocean/ionosphere parameter space. Key drivers of the ocean's induced response are its *conductivity*, *thickness*, and *depth* of the liquid layer below Triton's surface. The ocean models illustrated in Figure 6 (left) represent conductivity values ranging from 0.1 through 30 S/m (in log-linear increments) and thicknesses from 10 to 310 km in increments of 10 km.

Ocean conductivity is a function of the type and abundance of solutes that went into solution early in Triton's evolution, as well as the current solute concentration following top-down freezing of an icy shell. Conductivity—for which salinity is a proxy—is modeled based on a plausible range of initial ocean salinity values of 1–8 S/m (Castillo-Rogez et al., 2021). Increases in conductivity since initial ocean formation, including the possibility of saturation at  $\sim 24$  S/m as a bounding case (e.g., Rebello et al., 2020), are modeled to account for an initially thicker ocean freezing out and becoming thinner over time. Also modeled are additional parameters such as the water-to-rock ratio and temperature, which play a secondary role in determining how much of the volatiles combine into minerals (e.g.,  $\text{CO}_2$  in carbonates) are also modeled (Castillo-Rogez et al., 2021).

The induced signal from a conductive ocean depends on the ocean's conductance, the product of its conductivity and thickness. A constant overall thickness of Triton's hydrosphere (its ice layer plus the liquid ocean; Figure 5 right) of 340 km is assumed for this analysis, taking Io's density ( $\sim 3,500 \text{ kg/m}^3$ ) as a reference for Triton's core density, based on its likely dehydration following capture (Nimmo & Spencer, 2015). As a general rule, thinner oceans with lower conductivity are naturally the most difficult to detect because they induce a weaker signal at the point of measurement (the induced dipolar response decreases by  $1/r^3$ ).

The ocean models shown in blue within the dashed black line in Figure 6 (left) represent ocean characteristics most likely to be found at Triton based on these assumed geophysical parameters. Among this subset of the 256 models, the least-favorable likely ocean, shown as a green circle in this and subsequent figures, represents the

deepest of these oceans with the lowest conductivity: a thickness of 50 km, located 290 km below Triton's surface, with conductivity of 9 S/m (corresponding to an initial conductivity of 1 S/m prior to freezing).

To analytically explore the boundaries of ocean detectability with the PCA methodology in the presence of noise sources and plasma interaction fields, a significantly larger ocean parameter space than is currently considered likely from the geophysical perspective is defined. The ocean models shown in gray in Figure 6 (left) represent this artificial extension of the ocean parameter space beyond the blue ocean models considered likely to occur. Of this set of less likely cases, the least-favorable induced response would be from an extremely thin (10 km) ocean located 330 km below the surface of Triton, with a vanishingly small salinity of 0.1 S/m. Performance limits of the PCA methodology for these cases are shown in subsequent figures, in keeping with the blue/gray/green color scheme.

### 3.3. The Complex Response Function

The complex response function of a planetary body represents the amplitude and phase delay of the combined induction response of a particular ionosphere and ocean profile. Magnetic induction measurements are sensitive to ice-shell thickness and ocean depth, as the strength of an induced dipolar field degrades per  $(R_T/r)^3$ , where  $R_T$  is the radius of Triton and  $r$  is the radius to the observation. Algorithms for computing the magnetic induction response (see Equation 5) of concentrically stratified conductors, pioneered over 50 yr ago (Eckhardt, 1963) and recently matured (Vance et al., 2021), determine the specific induction response for each model via a height-integrated approach as shown in Figure 6 (right). Each shell has a unique conductivity and thickness. Although each specific shell typically has uniform conductivity, the ionosphere can be modeled with changing conductivity versus height to better represent unique and relatively intense ionospheres.

The radius of each shell is measured from Triton's center, including the mantle, the liquid ocean, ice layers, and the ionosphere up to an altitude of 800 km. The specific shell layer conductivity  $\sigma_n$  is also specified. The numerical approach employed provides the ability to solve for the complex response function using a configurable number of spherical shells of varying conductivity, to represent any layer of the atmosphere/ionosphere or interior to simulate conductivity gradients. This capability could be particularly beneficial for any trajectory that has the potential to measure the conductivity structure of the ionosphere. The resulting solution defines the unique induction response characteristics of a specific ionosphere and ocean model in the frequency domain:  $Q(f) = A(f)e^{-i\phi(f)}$ , where  $A$  is amplitude and  $\phi$  is phase delay relative to Neptune's driving AC magnetic field at frequency  $f$ . For all ocean worlds, phase delay—a characteristic of all electromagnetic signals that traverse through any ambient medium—is especially important for ocean detection. The differential phase delay between ocean and no-ocean cases is a distinctive factor in revealing the nature of the induced magnetic response. Using the 141-hr wave as an example, the ionosphere-only models characterized with low HIC exhibit a phase delay of roughly  $90^\circ$ , with a slight linear reduction with increasing HIC. However, all of the ocean-plus-ionosphere models are characterized with a phase delay of  $30^\circ$  or less, regardless of ionosphere HIC. Thus, the phase delay at the orbital period is a significant discriminating factor between the two model classes, even when their response amplitudes are similar. Additional plots are illustrated in Figure A1 of the Appendix to better illustrate these points, which are mathematically expressed by Equation 6 in the next section.

Figure 7 illustrates the complex response function  $A_k e^{-i\phi_k}$  for Neptune's dominant magnetic waves (with  $k$  indicative of discrete frequency), for the synodic 14-hr period and the 141-hr Triton orbital period, in a complex plane with real and imaginary axes for the large set of 13,056 ionosphere and ocean models defined in the parameter space. By contrast with Figure 1, there is now a clear separation of the ionosphere-only and ionosphere-plus-ocean model classes. The complex response function data for the 14-hr magnetic wave indicate that the primary synodic magnetic wave has limited penetration for an ionosphere intensity greater than  $\sim 40,000$  S, due to the low skin depth associated with a highly conducting ionosphere. This result indicates that detecting a potential subsurface ocean in the presence of an intense ionosphere depends primarily on the 141-hr orbital magnetic wave. The longer period of the 141-hr magnetic wave allows it to penetrate the full range of ionosphere intensities, with clear separation between the least-favorable likely ocean (green circle) and the ionosphere-only models (magenta–yellow). Primarily because of the dipolar field falloff, the response of deep, thin oceans with low salinity values of 0.1 S/m approaches that of the ionosphere-only models.

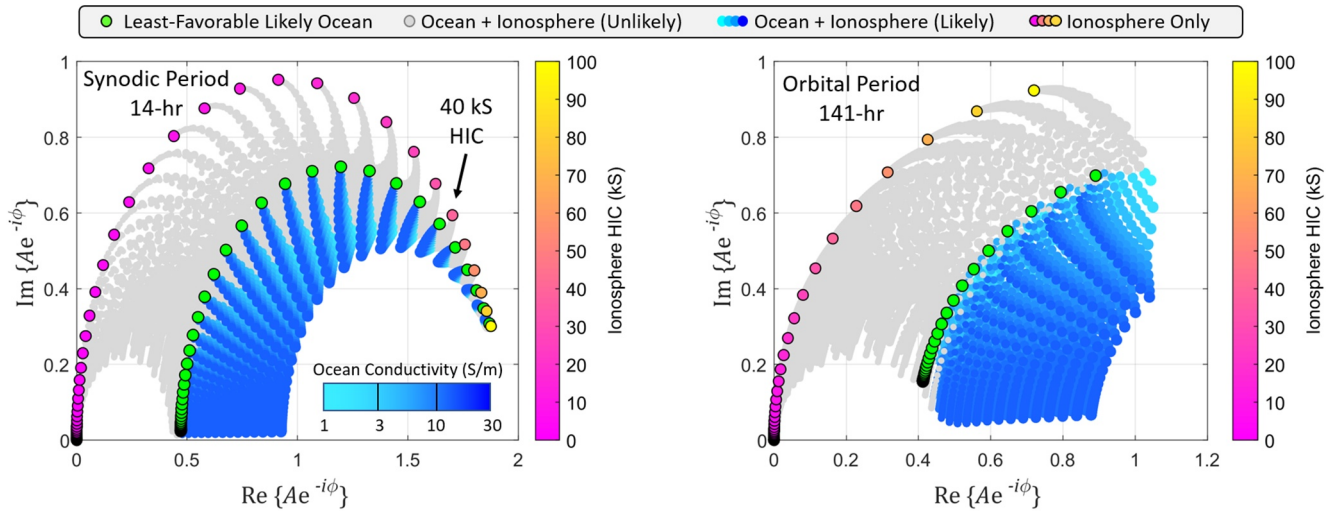


**Figure 7.** Triton's complex response functions evaluated at the frequencies corresponding to the synodic and orbital periods. (left) Complex plane representation of the complex response function for various combinations of ocean-plus-ionosphere models evaluated for the 14-hr synodic period of Neptune and the (right) 141-hr orbital period of Triton. The coloring of the ocean and ionosphere models corresponds to the scheme depicted in Figure 6. The green circles represent the least-favorable bounding case among the most likely ocean models, characterized by a thickness of 50 km and a conductivity of 9 S/m as depicted in Figure 6. Note that the ionosphere-only models and the ocean-plus-ionosphere models begin to overlay each other at the synodic period above ionosphere HIC of 40 kS, which stresses the usefulness of the orbital period where there is complete separation of model classes.

### 3.4. Total Induced Magnetic Moments

Ionosphere and ocean-induced MMs are responsible for the induced magnetic field that is measured by a passing spacecraft. This magnetic field along the trajectory, in units of nT, is forward modeled using the real part of the dipole field equation defined by:

$$\mathbf{B}_{\text{Ind}}(\mathbf{r}, t) = \text{Re} \left\{ \frac{\mu_0}{4\pi} \frac{3(\mathbf{r}(t) \cdot \mathbf{U}(t))\mathbf{r}(t) - r^2(t) \mathbf{U}(t)}{r^5(t)} \right\}. \quad (3)$$

Here,  $\mathbf{r}(t) = [x(t), y(t), z(t)]$  is the position of the spacecraft with respect to the center of the moon and  $\mathbf{U}(t)$  is the induced MM vector in units of A-m<sup>2</sup>, based on an induction model initially applied to the Jovian moons (Zimmer et al., 2000), defined by:

$$\mathbf{U}(t) = \frac{4\pi}{\mu_0} \frac{R_T^3}{2} \mathbf{M}(t), \quad (4)$$

where  $\mu_0$  is the permeability of free space,  $R_T$  is the radius of Triton (1,353.4 km), and the time-varying portion of the moment vector  $\mathbf{M}(t) = [M_x(t), M_y(t), M_z(t)]$ , in units of nT, is defined by:

$$\mathbf{M}(t) = - \sum_k A_k e^{-i\phi_k} \mathbf{B}_{N,k}(t). \quad (5)$$

The summation of terms in Equation 5 represents the total induced MM driven by Neptune's AC magnetic field  $\mathbf{B}_{N,k}(t)$  at the 15 discrete frequencies  $k$ , although the two primary (synodic and orbital) frequencies dominate. The complex response function  $A_k e^{-i\phi_k}$  represents a specific ionosphere-only or ionosphere-plus-ocean model where  $A_k$  is the relative amplitude and  $\phi_k$  is the phase delay or lag of the model's induction response at frequency  $k$  with respect to that which would be induced by a perfectly conducting sphere of radius  $R_T$ .

The real part of these MMs can be represented by the summation of phase-delayed dominant magnetic waves at various frequencies (see top right panel of Figure 4) multiplied by the amplitude of the associated complex response function:

$$M_x(t) = - \sum_k A_k B_{x,k} \cos(2\pi f_k t + \theta_{x,k} - \phi_k),$$

$$M_y(t) = - \sum_k A_k B_{y,k} \cos(2\pi f_k t + \theta_{y,k} - \phi_k), \quad (6)$$

$$M_z(t) = - \sum_k A_k B_{z,k} \cos(2\pi f_k t + \theta_{z,k} - \phi_k).$$

The strength of the MMs is directly related to the amplitude of the complex response function  $A_k$  and the associated driving magnetic field strength of the specific  $k$  frequencies. However, the phase delay  $\phi_k$  is also important in determining the strength of the MMs associated with ionosphere-only and ocean-plus-ionosphere models, and thus for discerning contributions of an ocean to the overall induction response.

### 3.5. Induced Dipole Magnetic Field Time-Series

To aid in the analysis, the magnetic induction fields (Equation 3) are written conveniently in matrix notation. The forward modeling of the 13,056 induced magnetic field time-series illustrated in Figure 1,  $B_{\text{ind},x}(t)$ ,  $B_{\text{ind},y}(t)$ , and  $B_{\text{ind},z}(t)$  can be expressed as a matrix multiplication of the dipolar matrix  $\mathbf{D}(t)$  and the total MM matrix  $\mathbf{M}(t)$ :

$$\mathbf{B}_{\text{Ind}}(t) = \mathbf{D}(t)\mathbf{M}(t), \quad (7)$$

where the 3-by-3 dipolar trajectory matrix is defined at time  $t$ :

$$\mathbf{D}(t) = \frac{R_T^3}{2} \frac{1}{r(t)^5} \begin{bmatrix} 3x(t)^2 - r(t)^2 & 3x(t)y(t) & 3x(t)z(t) \\ 3y(t)x(t) & 3y(t)^2 - r(t)^2 & 3y(t)z(t) \\ 3z(t)x(t) & 3z(t)y(t) & 3z(t)^2 - r(t)^2 \end{bmatrix}. \quad (8)$$

Because the velocity of the spacecraft is fast relative to changes in the magnetic waves experienced by Triton over the 12-min encounter, the MM vector is essentially stationary over the duration of the encounter and can be approximated as a 3-element vector  $\mathbf{M} = [M_x(t_{ca}), M_y(t_{ca}), M_z(t_{ca})]$  where  $t_{ca}$  represents the spacecraft's time at closest approach to Triton. Assuming the magnetometer acquires samples at a rate of  $F_s$  samples/second, the discrete-time representation of the dipolar field time-series is formed by the substitution  $t = nT_s$ , where  $n$  is the sample index and  $T_s = 1/F_s$  the sampling period in units of seconds. Equation 7 now becomes:

$$\begin{bmatrix} B_{\text{ind},x}(n) \\ B_{\text{ind},y}(n) \\ B_{\text{ind},z}(n) \end{bmatrix} = \begin{bmatrix} D_{11}(n) & D_{12}(n) & D_{13}(n) \\ D_{21}(n) & D_{22}(n) & D_{23}(n) \\ D_{31}(n) & D_{32}(n) & D_{33}(n) \end{bmatrix} \begin{bmatrix} M_x(n) \\ M_y(n) \\ M_z(n) \end{bmatrix}, \quad \text{with } n = 1 \text{ to } N \quad (9)$$

A detailed ocean classification space, defined by the MMs at closest approach  $M_x$ ,  $M_y$ , and  $M_z$ , represents the unique attributes of a range of potential sub-surface oceans and/or ionospheric profiles. In the absence of noise, each model in the classification space is unique and represents specific physical parameters (e.g., ice shell thickness, ocean thickness and conductivity, and ionospheric conductance). The figure of merit for ocean detection in this work is referred to as  $MS$ , defined as the three-dimensional Euclidean distance between the corresponding total induced MMs of the ionosphere-only and ocean-plus-ionosphere models, measured in units of nT. The  $M_z$  components of the total MMs is small but does contribute to the separation of model classes. The left panel of Figure 8 illustrates the MM classification space (only  $M_x$  and  $M_y$  shown) of the 13,056 forward models used in this study, computed using the 15 most dominant discrete magnetic waves (per Equations 5 and 6). The  $MS$  of ocean-plus-ionosphere to ionosphere-only models is illustrated in the right panel of Figure 8, plotted as a function of ionosphere HIC from 0 to 100,000 S. The ocean classification space presented in the figure represents the classification space of Path 1 of Figure 2 for an assumed 14-hr magnetic phase of zero (defined by Connerney et al., 1991). For an ionosphere HIC greater than  $\sim 50,000$  S,  $MS$  drops below 1 nT which can be challenging for classification purposes in the presence of noise, especially when the full range of 14-hr magnetic phase is considered (Section 6.2). Thus, Section 4 focuses on increasing  $MS$  of the model classes using a concept called *SMMs*, which is equivalent to the separation achieved by PCA (see Section 5).

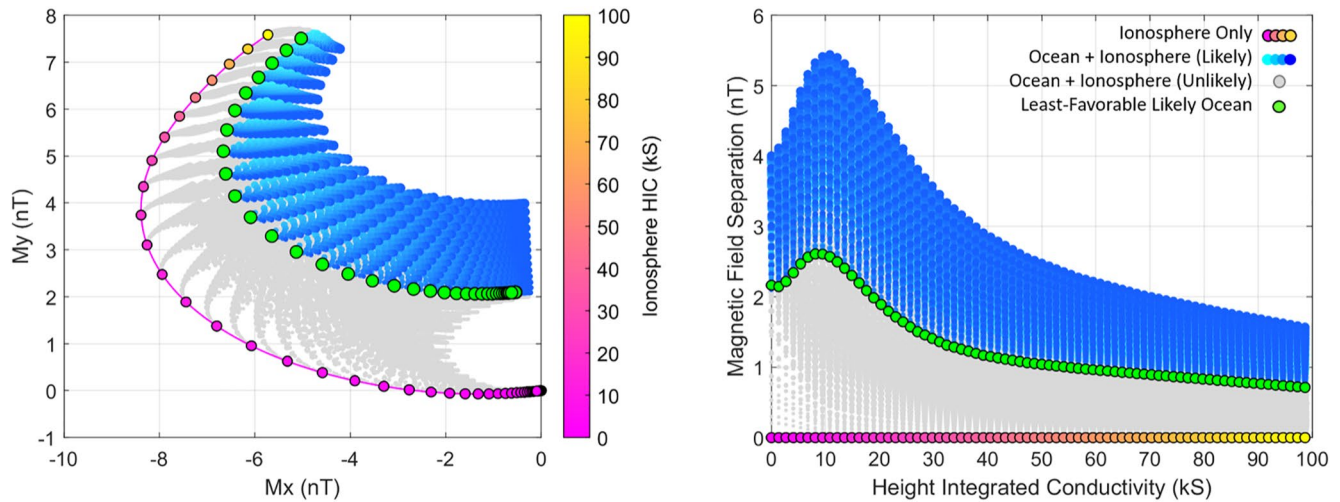


**Figure 8.** Ocean classification space defined by the induced magnetic moments. (left)  $M_x$  and  $M_y$  magnetic moment components for all forward modeled cases. (Note that there is also a third dimension representing the  $M_z$  component that is not shown due to its relatively small magnitude relative to the other two components.) (right) The magnetic separation between ionosphere-only and ocean-plus-ionosphere magnetic moments for all models as a function of ionosphere HIC.

#### 4. Scaled Magnetic Moments (SMM)

As previously described, Path 2 of Figure 2 entails using PCA to directly process the induced magnetic field time-series  $B_{\text{Ind},x}(n)$ ,  $B_{\text{Ind},y}(n)$ , and  $B_{\text{Ind},z}(n)$ . This approach leads to the concept of *SMMs* discussed in this section.

##### 4.1. Preservation of Signal Energy

MS between distinct data classes can be increased when the signal energy, or the *spread* of the data (analogous to its standard deviation), associated with the induced dipolar field discrete time-series is retained in the analysis. The total discrete-time signal energy  $E_{\text{signal}}$  contained in the time-series can be compactly written in terms of a SMM vector:

$$E_{\text{signal}} = \sum_{n=1}^N [B_{\text{Ind},x}^2(n) + B_{\text{Ind},y}^2(n) + B_{\text{Ind},z}^2(n)] = M_1^2 + M_2^2 + M_3^2, \quad (10)$$

where the SMM vector  $[M_1, M_2, M_3]$  is simply related to the time-varying portion of the induced MM vector  $[M_x, M_y, M_z]$  of the forward model through a 3-by-3 scaling matrix  $S_{\text{SMM}}$ :

$$\begin{bmatrix} M_1 \\ M_2 \\ M_3 \end{bmatrix} = \begin{bmatrix} S_{11} & S_{12} & S_{13} \\ S_{21} & S_{22} & S_{23} \\ S_{31} & S_{32} & S_{33} \end{bmatrix} \begin{bmatrix} M_x \\ M_y \\ M_z \end{bmatrix}. \quad (11)$$

The closed form notation of Equation 11 indicates the possibility of viewing the induced dipolar fields in a reduced dimensionality, suggesting that PCA provides a viable methodology to perform this task. As will be shown in Section 5, the PCs produced by PCA are directly related to the SMM detailed here, and effectively result in identical MS of ionosphere-only and ocean-plus-ionosphere model classes.

By multiplying out Equation 11 and inserting into Equation 10, the coefficients of the 9-element scaling matrix  $S_{\text{SMM}}$  can be solved for analytically. Because there are 9 unknowns and 6 equations, the resulting system is under-determined. However, the scaling matrix can be readily constrained to be symmetrical about the diagonal (e.g., off-diagonal terms are mirrored) or more conveniently, 3 of the 9 elements simply set to zero. The coefficients are defined by:

$$S_{11} = \sqrt{C_{xx}} \quad (12a)$$

$$S_{12} = C_{xy}/\sqrt{C_{xx}} \quad (12b)$$

$$S_{13} = C_{xz}/\sqrt{C_{xx}} \quad (12c)$$

$$S_{22} = (C_{yy} - S_{12}^2)^{1/2} \quad (12d)$$

$$S_{23} = (C_{yz} - S_{12}S_{13}/C_{xx})/S_{22} \quad (12e)$$

$$S_{33} = (C_{zz} - S_{13}^2 - S_{23}^2)^{1/2} \quad (12f)$$

$$S_{21} = S_{31} = S_{32} = 0, \quad (12g)$$

where the constants  $C_{xx}$ ,  $C_{yy}$ ,  $C_{zz}$ ,  $C_{xy}$ ,  $C_{xz}$ , and  $C_{yz}$  are defined by:

$$C_{xx} = \sum_{n=1}^N [D_{11}(n)^2 + D_{21}(n)^2 + D_{31}(n)^2] \quad (13a)$$

$$C_{yy} = \sum_{n=1}^N [D_{12}(n)^2 + D_{22}(n)^2 + D_{32}(n)^2] \quad (13b)$$

$$C_{zz} = \sum_{n=1}^N [D_{13}(n)^2 + D_{23}(n)^2 + D_{33}(n)^2] \quad (13c)$$

$$C_{xy} = \sum_{n=1}^N [D_{11}(n)D_{12}(n) + D_{21}(n)D_{22}(n) + D_{31}(n)D_{32}(n)] \quad (13d)$$

$$C_{xz} = \sum_{n=1}^N [D_{11}(n)D_{13}(n) + D_{21}(n)D_{23}(n) + D_{31}(n)D_{33}(n)] \quad (13e)$$

$$C_{yz} = \sum_{n=1}^N [D_{12}(n)D_{13}(n) + D_{22}(n)D_{23}(n) + D_{32}(n)D_{33}(n)]. \quad (13f)$$

#### 4.2. Magnetic Separation of Scaled Magnetic Moments

A key figure of merit of the proposed ocean detection methodology involves the MS of two model classes in a multi-dimensional space  $[MS_1, MS_2, MS_3]$ . This MS can be directly calculated with the use of the scaling matrix  $S_{SMM}$  (with coefficients given by Equation 12) and the MS between ocean and no-ocean MMs  $[MS_x, MS_y, MS_z]$ , represented in Figure 8:

$$\begin{bmatrix} MS_1 \\ MS_2 \\ MS_3 \end{bmatrix} = \begin{bmatrix} S_{11} & S_{12} & S_{13} \\ 0 & S_{22} & S_{23} \\ 0 & 0 & S_{33} \end{bmatrix} \begin{bmatrix} M_{x,Ocean} - M_{x,Ion} \\ M_{y,Ocean} - M_{y,Ion} \\ M_{z,Ocean} - M_{z,Ion} \end{bmatrix} = \begin{bmatrix} S_{11} & S_{12} & S_{13} \\ 0 & S_{22} & S_{23} \\ 0 & 0 & S_{33} \end{bmatrix} \begin{bmatrix} MS_x \\ MS_y \\ MS_z \end{bmatrix}, \quad (14)$$

where  $[M_{x,Ocean}, M_{y,Ocean}, M_{z,Ocean}]$  corresponds to the MM associated with a representative ocean-plus-ionosphere model and  $[M_{x,Ion}, M_{y,Ion}, M_{z,Ion}]$  corresponds to the MM of the associated ionosphere model it was convolved with. Figure 9 (left) illustrates the scaled total MMs—for brevity abbreviated SMM—compared to the total MMs that would be obtained in Path 1 of Figure 2. The ionosphere-only models are compared to those for the ionospheres convolved with the least-favorable likely ocean cases (green circles) across the ionosphere intensity range of 0–100,000 S. Figure 9 (right) compares MS across this intensity range, assuming a magnetometer sampling rate of one sample per second. Note that the SMMs exhibit significantly increased separation compared to the original MMs obtained through Path 1 of Figure 2. As a foreshadowing of the PCA results discussed in the next section, the PCs of the dipolar field time-series are also shown in the figure and, as illustrated, result in *identical* MS to that of the SMMs. The PCA results exhibit a rotation as compared with the SMM data derived in Equation 14, but this is simply a characteristic of the tool and is not relevant to the separation between model classes and hence ocean detection. The rotation occurs because PCA maximizes data variability for its primary principal component axis (PC1), followed by PC2 and then PC3.

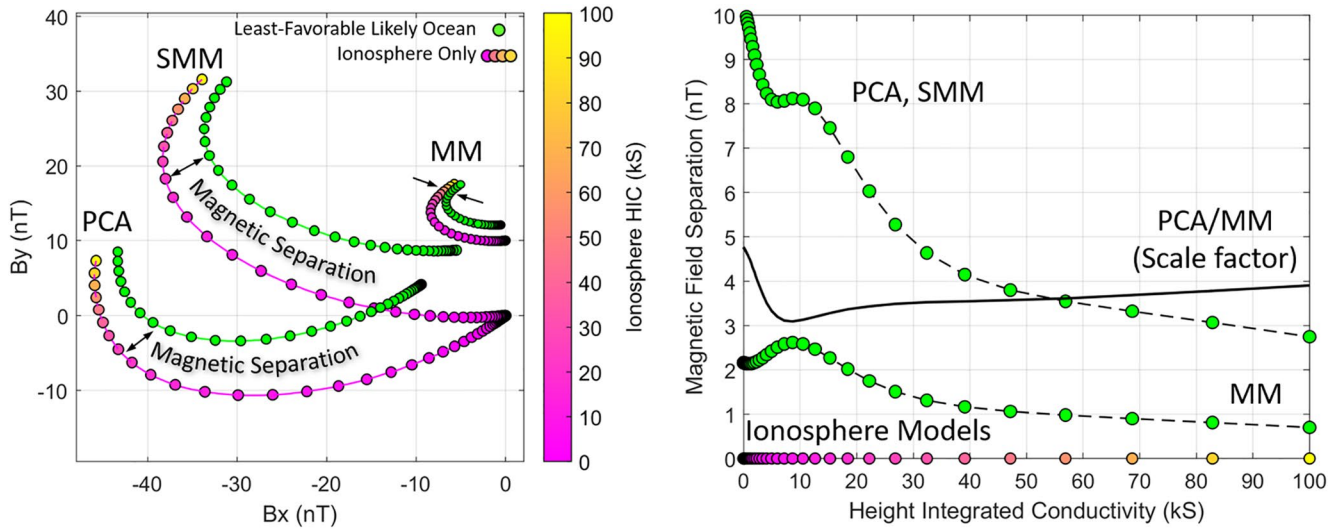


**Figure 9.** Data dimensionality reduction of the induced magnetic field time-series results in increased magnetic separation compared to that exhibited by the induced magnetic moments. (left) Comparison of the magnetic separation for the magnetic moments (MM, offset in +y by 10 nT for visual clarity), scaled magnetic moments (SMM) acquired by the analytical approach, and PCA method for all of the ionosphere-only models (magenta) and ionosphere-plus-ocean models relative to the least-favorable bounding ocean case (green), with thickness of 50 km and 9 S/m conductivity. (right) Plot of magnetic separation (distance measured in a 3-dimensional space) achieved by each of the three methods. Note that the analytical approach exactly replicates the magnetic separation achieved by PCA. Also note the increase in separation achieved by PCA, represented in terms of the scale factor by the black solid line.

#### 4.3. Linear Transform of the Induced Dipole Field Time-Series to $M_1$ , $M_2$ , and $M_3$

The dipolar induction fields noted by Equation 9 can be expressed conveniently in matrix form by  $\mathbf{B} = \mathbf{D}\mathbf{M}$  for all time  $t$ , written in expanded form by:

$$\begin{bmatrix} B_{\text{Ind},x}(1) \\ \vdots \\ B_{\text{Ind},x}(N) \\ B_{\text{Ind},y}(1) \\ \vdots \\ B_{\text{Ind},y}(N) \\ B_{\text{Ind},z}(1) \\ \vdots \\ B_{\text{Ind},z}(N) \end{bmatrix} = \begin{bmatrix} D_{11}(1) & D_{12}(1) & D_{13}(1) \\ \vdots & \vdots & \vdots \\ D_{11}(N) & D_{12}(N) & D_{13}(N) \\ D_{21}(1) & D_{22}(1) & D_{23}(1) \\ \vdots & \vdots & \vdots \\ D_{21}(N) & D_{22}(N) & D_{23}(N) \\ D_{31}(1) & D_{32}(1) & D_{33}(1) \\ \vdots & \vdots & \vdots \\ D_{31}(N) & D_{32}(N) & D_{33}(N) \end{bmatrix} \begin{bmatrix} M_x \\ M_y \\ M_z \end{bmatrix}. \quad (15)$$

Matrix  $\mathbf{B}$  is a  $3N$ -by-1 vector representing the component interleaved induced magnetic field time-series  $\mathbf{B}_{\text{Ind}}(n)$  and  $\mathbf{D}$  is a  $3N$ -by-3 matrix which represents the dipolar matrix terms of Equation 9.  $\mathbf{M} = [M_x, M_y, M_z]$  is the associated time-varying portion of the MM vector, assumed to be static at closest approach, expressed as a 3-by-1 vector. This vector can be solved via least squares inversion, effectively by taking the product of the pseudo-inverse of the matrix  $\mathbf{D}$  and the magnetic field time-series  $\mathbf{B}$ :

$$\mathbf{M} = [(\mathbf{D}'\mathbf{D})^{-1}\mathbf{D}']\mathbf{B}. \quad (16)$$

Using this estimate of the MM, the SMM vectors  $[M_1, M_2, M_3]$  are computed by multiplying through with the derived scaling matrix  $\mathbf{S}_{\text{SMM}}$ , with coefficients defined by Equation 12:

$$\begin{bmatrix} M_1 \\ M_2 \\ M_3 \end{bmatrix} = \mathbf{S}_{\text{SMM}}[(\mathbf{D}'\mathbf{D})^{-1}\mathbf{D}']\mathbf{B} = \mathbf{V}_{\text{SMM}}\mathbf{B} = \begin{bmatrix} v_1(1) & \dots & v_1(3N) \\ v_2(1) & \dots & v_2(3N) \\ v_3(1) & \dots & v_3(3N) \end{bmatrix} \begin{bmatrix} B_{\text{Ind},x}(1) \\ \vdots \\ B_{\text{Ind},x}(N) \\ B_{\text{Ind},y}(1) \\ \vdots \\ B_{\text{Ind},y}(N) \\ B_{\text{Ind},z}(1) \\ \vdots \\ B_{\text{Ind},z}(N) \end{bmatrix}, \quad (17)$$

yielding an equivalent 3-by-3N projection matrix (similar to the PCA eigenvectors discussed in subsequent sections) defined by  $\mathbf{V}_{\text{SMM}} = \mathbf{S}_{\text{SMM}}(\mathbf{D}'\mathbf{D})^{-1}\mathbf{D}'$ . Equation 17 can now be used to project a forward-modeled magnetic field time-series (or a noisy measurement) into the SMM classification space, similar to that illustrated in Path 2 of Figure 2.

## 5. Principal Component Analysis (PCA)

### 5.1. PCA Design Matrix

PCA is a powerful data dimensionality reduction technique that has been extensively used for feature extraction and classification in a wide variety of scientific and engineering disciplines (Alken et al., 2017; Hannachi et al., 2007; Jolliffe & Cadima, 2016), but has not been previously applied to magnetic induction data sets for planetary ocean detection or characterization. The power of PCA lies in its ability to identify patterns and correlation between features in large, complex data sets such as the forward modeled magnetic field time-series data. The method aims to find the axes of maximum variance in high-dimensional data (the number of samples  $N$  over time being the dimension in this case) and projects it onto a new subspace of PCs with fewer dimensions using a linear transformation. For ocean detection purposes, PCA provides a classification space that defines two distinct clusters of ocean-plus-ionosphere and ionosphere-only models, which can be distinguished by a 3-dimensional boundary, based on PCs of the induced dipolar field time-series. PCA projects the 13,056 forward modeled magnetic induction fields into the classification space defined by  $\text{PC}_1$ ,  $\text{PC}_2$ , and  $\text{PC}_3$  as illustrated in Path 2 of Figure 2. This three-dimensional classification space yields identical magnetic field separation between the two model classes as the SMMs ( $M_1, M_2, M_3$ ) presented in the previous section.

PCA provides the additional benefit of being able to process the measurements made from the magnetometer directly after subtraction of the Neptune background field. Additional flexibility is gained in that not all magnetometer channels are required for ocean detection purposes (see Section 7.1), additional ocean discrimination occurs, and improved characterization is achieved for multiple flybys (Sections 6.3 and 9).

The first step in the PCA ocean detection algorithm is concatenating the three channels of the induced dipolar magnetic field time-series (each  $N$  samples long) for each of the  $P$  forward models (13,056 in this analysis) to form a matrix as input. The  $3N$  samples for each of the  $P$  forward models are stored vertically in a matrix  $\mathbf{Y}$  with dimension  $3N$ -by- $P$  as illustrated in Equation 18a. These data are centered by subtracting out the mean across each row time index to create a design matrix  $\mathbf{X}$  (Equation 18b). Figure 10 (top) illustrates the centered three channels of the forward modeled induced dipolar magnetic field time-series (each  $N$  samples long and with the background field removed) for all ionosphere-only (magenta) and ocean-plus-ionosphere (shades of blue) models, in addition to a representative noisy measurement (orange). The matrix denoted by Equation 18b is directly input into the PCA ocean detection routine:

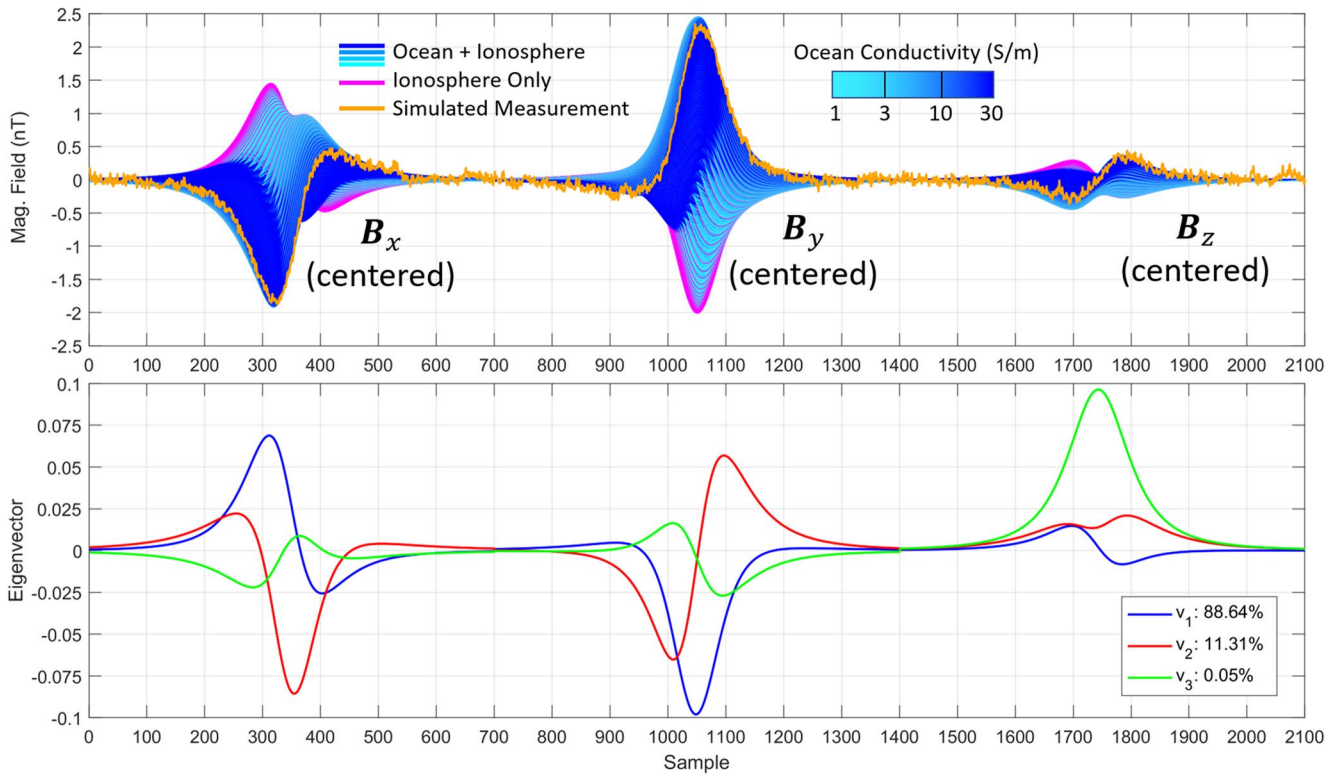


**Figure 10.** The eigenvector decomposition results in a set of eigenvectors that resemble the structure of the induced magnetic field time-series. (top) Columns of the design matrix  $\mathbf{X}$ , formed from the centered magnetic induction fields of the forward modeled ocean-plus-ionosphere (blue) and ionosphere-only (magenta) models, plotted as a function of sample number. Also plotted in the panel is a representative noisy measurement of the induced magnetic field components (orange), concatenated and centered. (bottom) The top three eigenvectors extracted from the covariance matrix. Here,  $v_1$  explains 88.64% of the data variance,  $v_2$  explains 11.31% of the data variance, and  $v_3$  explains 0.05% of the data variance.

$$\mathbf{Y} = \begin{bmatrix} B_{\text{Ind},x,1}(1) & \cdots & B_{\text{Ind},x,P}(1) \\ \vdots & & \vdots \\ B_{\text{Ind},x,1}(N) & \cdots & B_{\text{Ind},x,P}(N) \\ B_{\text{Ind},y,1}(1) & \cdots & B_{\text{Ind},y,P}(1) \\ \vdots & & \vdots \\ B_{\text{Ind},y,1}(N) & \cdots & B_{\text{Ind},y,P}(N) \\ B_{\text{Ind},z,1}(1) & \cdots & B_{\text{Ind},z,P}(1) \\ \vdots & & \vdots \\ B_{\text{Ind},z,1}(N) & \cdots & B_{\text{Ind},z,P}(N) \end{bmatrix} \quad (18a)$$

$$\mathbf{X} = \begin{bmatrix} B_{\text{Ind-C},x,1}(1) & \cdots & B_{\text{Ind-C},x,P}(1) \\ \vdots & & \vdots \\ B_{\text{Ind-C},x,1}(N) & \cdots & B_{\text{Ind-C},x,P}(N) \\ B_{\text{Ind-C},y,1}(1) & \cdots & B_{\text{Ind-C},y,P}(1) \\ \vdots & & \vdots \\ B_{\text{Ind-C},y,1}(N) & \cdots & B_{\text{Ind-C},y,P}(N) \\ B_{\text{Ind-C},z,1}(1) & \cdots & B_{\text{Ind-C},z,P}(1) \\ \vdots & & \vdots \\ B_{\text{Ind-C},z,1}(N) & \cdots & B_{\text{Ind-C},z,P}(N) \end{bmatrix}. \quad (18b)$$

### 5.2. PCA Covariance Matrix and Eigenvectors

The next step in the method is computing the covariance matrix, defined by  $\mathbf{X}\mathbf{X}'$ , which has dimension  $3N$ -by- $3N$ . PCA effectively performs an eigenvalue decomposition of the covariance matrix, which yields a set of eigenvectors  $\mathbf{V}_{\text{PCA}}$ , each of length  $3N$ , defined by:

$$\mathbf{V}_{\text{PCA}} = \begin{bmatrix} v_1(1) & \cdots & v_{3N}(1) \\ \vdots & & \vdots \\ v_1(3N) & \cdots & v_{3N}(3N) \end{bmatrix}. \quad (19)$$

The PCA eigenvectors represent the axes of greatest variability, where the amount of variability is defined by its associated eigenvalue. The  $\text{PC}_1$  eigenvector represents the basis transformation associated with the axis of greatest variance in the data and is used to project the data into the new lower-dimension classification space. Thus, the signal variation associated with  $\text{PC}_1$  will always be the highest and contain the most information (e.g., signal variance). As the three eigenvectors associated with the largest three eigenvalues represent more than 99.99% of the variation of the data for a single flyby, retention of only those three is sufficient to accurately project the high dimensionality data contained in the design matrix  $\mathbf{X}$  onto the 3-dimension PC classification space. These three eigenvectors,  $v_1$ ,  $v_2$ , and  $v_3$ , are plotted as a function of sample number in the bottom panel of Figure 10. Note the similarity of the line shapes of the eigenvectors with those of the induced magnetic field responses illustrated in the upper panel. It is the dipolar matrix that results in the unique shape of the magnetic induction fields in the top panel of Figure 10, as the MMs are near-constant as a result of the relatively short encounter time (12-min). The dipolar matrix is also common to all of the PCA input data. As such, the shape of the dipolar matrix coefficients as a function of time governs the shape of the eigenvectors extracted from the covariance matrix.

### 5.3. Linear Transform of Induced Dipole Field Time-Series to PC1, PC2, and PC3

Without any loss of information, the PCs associated with each of the  $P$  models are computed by the projection operation,  $\mathbf{PC} = \mathbf{V}'_{\text{PCA}}\mathbf{X}$ , and the top three PCs ( $\text{PC}_1$ ,  $\text{PC}_2$ ,  $\text{PC}_3$ ) are retained for each model as they contain all of the information in the time-series. The PCs associated with the  $p$ th model are computed by:

$$\mathbf{PC}_p = \mathbf{V}'_{\text{PCA}}\mathbf{X}_p = \begin{bmatrix} \text{PC}_{1,p} \\ \text{PC}_{2,p} \\ \text{PC}_{3,p} \end{bmatrix} = \begin{bmatrix} v_1(1) & \cdots & v_1(3N) \\ v_2(1) & \cdots & v_2(3N) \\ v_3(1) & \cdots & v_3(3N) \end{bmatrix} \begin{bmatrix} B_{\text{Ind-C},1,p} \\ \vdots \\ B_{\text{Ind-C},3N,p} \end{bmatrix} \quad (20)$$

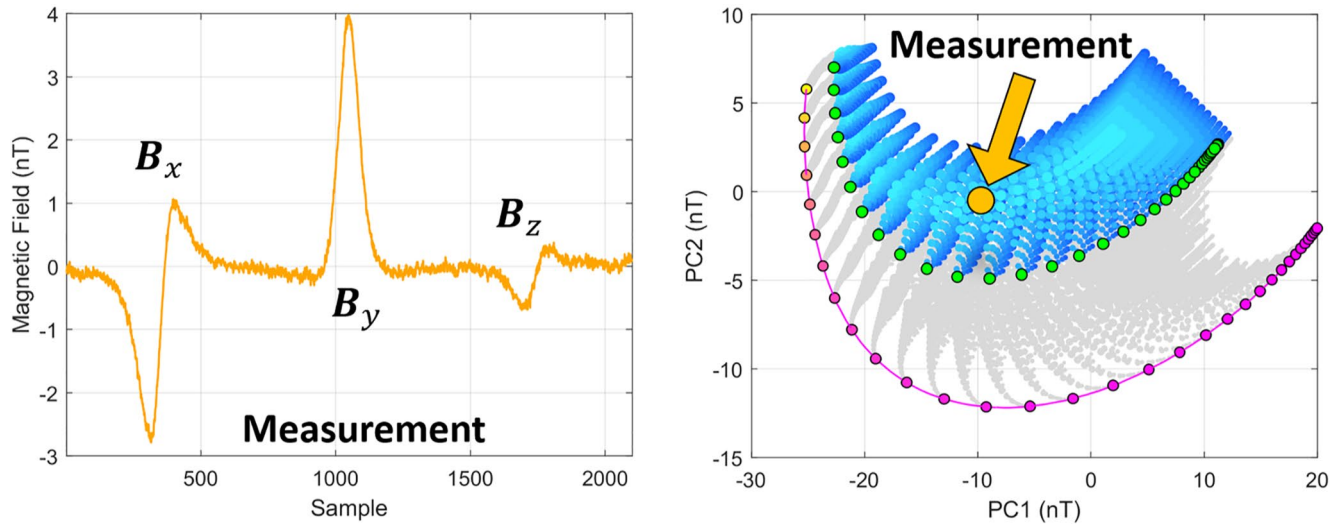


**Figure 11.** Representation of how a measurement gets projected into the PC classification space. (left) A representative noisy measurement of the induced magnetic field from components in concatenated format of an ocean model and (right) depiction of where this measurement gets projected in the PC space defined by the noise-free models.

where  $X_p$  represents the  $p$ th column in  $X$ . When an actual (noisy) observation is made from a spacecraft in the vicinity of the potential ocean world, the planetary background field is subtracted using a polynomial fitting routine as a first processing step, the three magnetometer channels are concatenated and centered to form the vector  $X_M$  ( $M$  for measurement), and then projected into the reduced dimension PC classification space using the eigenvectors  $V_{\text{PCA}}$  associated with the noise-free forward modeled data,  $PC_M = V'_{\text{PCA}} X_M$ . Figure 11 conceptualizes the projection of the representative noisy simulated observation, colored in orange, into the classification space defined by all the other  $P$  forward models.

It should be pointed out that not only does this methodology serve as a binary classifier of ocean versus no-ocean outcomes, but it also serves as a tool for characterization of ocean properties. The absolute position in PC space provides a direct correspondence to ocean and ionosphere parameters because each forward modeled ocean represents a unique interior configuration. Thus, depending on where the projected measurement lands in the classification space, inferences can be made regarding key ocean properties such as ocean thickness and conductivity. The amount of noise on the measurements will dictate the constraints that can be placed on these key interior parameters and will be discussed in Section 7.2.

#### 5.4. Comparison: PCA, SMMs, and Total MMs

Figure 12 illustrates the classification spaces (only two of three dimensions shown) for PCA, SMMs and the total MMs, all plotted on the same scale to emphasize the similarities and differences. Also plotted on the same scale are the associated ionospheric MS plots achieved for each analysis method. As illustrated, the PCA and SMM spaces look very similar and result in identical MS, which are both scaled compared to the total MMs. As noted earlier, the only difference between PCA and SMM is a rotation of the data space, mainly in PC1 and PC2, which does not impact the MS between the two model classes.

By reducing the dimensionality of the induced dipolar field time-series for both forward modeled data and the actual measurements, PCA allows for easy interpretation of the observations. No information is added or discarded. PCA simply *reorganizes* the data based on the inherent separation of the SMMs, noting that the dipolar matrix is common to all the forward models and the measurement. It can be shown that the projection operation achieved by PCA (using the top three eigenvectors) reduces to a simple 3-by-3 matrix that scales and rotates the MM vector for each of the  $P$  models. The PCA scaling matrix  $S_{\text{PCA}}$  can also be directly related to the eigenvectors and the dipolar matrix as illustrated by:

$$PC_p = V'_{\text{PCA}} X_p = V'_{\text{PCA}} (DM_p) = (V'_{\text{PCA}} D) M_p = S_{\text{PCA}} M_p, \quad (21)$$

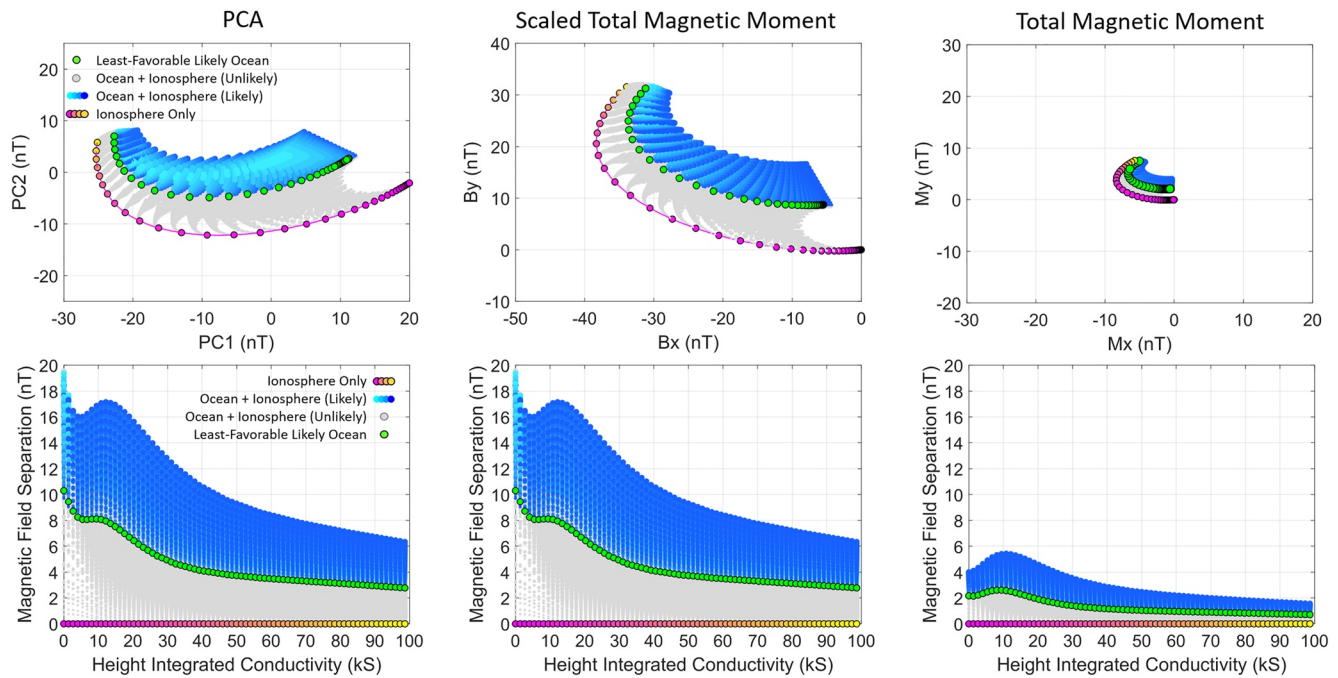


**Figure 12.** PCA provides an enhancement in magnetic separation compared to the total magnetic moments, enabled by the retention of all the data. Comparison of the (left panels) PCA, (middle panels) scaled magnetic moment (SMM), and (right panels) total magnetic moment classification spaces and their associated ocean-to-ionosphere magnetic separation plots. Note also that the magnetic separation across the ionosphere HIC range achieved by PCA is identical to that of the SMM.

and in expanded matrix form illustrated by:

$$\mathbf{PC}_p = \begin{bmatrix} \text{PC}_{1,p} \\ \text{PC}_{2,p} \\ \text{PC}_{3,p} \end{bmatrix} = \begin{bmatrix} v_1(1) & \cdots & v_1(3N) \\ v_2(1) & \cdots & v_2(3N) \\ v_3(1) & \cdots & v_3(3N) \end{bmatrix} \begin{bmatrix} D_{11}(1) & D_{12}(1) & D_{13}(1) \\ \vdots & \vdots & \vdots \\ D_{11}(N) & D_{12}(N) & D_{13}(N) \\ D_{21}(1) & D_{22}(1) & D_{23}(1) \\ \vdots & \vdots & \vdots \\ D_{21}(N) & D_{22}(N) & D_{23}(N) \\ D_{31}(1) & D_{32}(1) & D_{33}(1) \\ \vdots & \vdots & \vdots \\ D_{31}(N) & D_{32}(N) & D_{33}(N) \end{bmatrix} \begin{bmatrix} M_{x,p} \\ M_{y,p} \\ M_{z,p} \end{bmatrix} = \begin{bmatrix} S_{11} & S_{12} & S_{13} \\ S_{21} & S_{22} & S_{23} \\ S_{31} & S_{32} & S_{33} \end{bmatrix} \begin{bmatrix} M_{x,p} \\ M_{y,p} \\ M_{z,p} \end{bmatrix}. \quad (22)$$

As previously stated, the scaling matrices in Equations 11–13 ( $S_{\text{SMM}}$ ) and 21–22 ( $S_{\text{PCA}}$ ) can be related by a translation and a set of rotations.

## 6. Sensitivity to Trajectory and Time-of-Arrival

### 6.1. Sensitivity to Trajectory Approach Angle

Now that it has been demonstrated that MS can be increased between the two model classes by retaining the signal energy contained in the dipolar field time-series, it is important to further investigate the ramifications of a specific trajectory. For the single flyby case, the scalings of both matrices  $S_{\text{PCA}}$  and  $S_{\text{SMM}}$  are independent

of the MMs, and are dependent on the dipolar matrix terms  $D$  (dictated by the trajectory) and the number of samples in the magnetic field time-series. Within the limits imposed by signal noise (see Section 7.2), MS can be increased by increasing the number of samples  $N$ . As defined by the dominant diagonal scaling terms, an increase in the sample rate by a factor  $K$  results in an increase in the scale factor of  $\sqrt{K}$ . Note that reducing the encounter velocity also results in an improved scale factor as more samples can be acquired from the magnetometer given the same sampling rate. The dipolar matrix (Equation 8) indicates that reducing the positional vector  $r(t)$  at closest approach also increases the scaling factor as the magnetometer is effectively sampling stronger induction fields.

Independent of the scaling matrices associated with the dipolar matrix, the orbital phase of Triton along its highly inclined circular orbit (i.e., argument of latitude, AoL) during the spacecraft flyby affects the strength and orientation of the MMs as defined in Equation 6. An ideal encounter would occur *near* the highest or lowest position of Triton in its orbit where the 141-hr wave is maximized (see Figure 4), corresponding to an AoL of  $90^\circ$  or  $270^\circ$ , especially for an ionosphere HIC value above 50,000 S where the 141-hr orbital magnetic wave is the primary driver of magnetic induction within the ocean. However, depending on the ocean model and ionosphere HIC parameters, the 141-wave maximum MS can vary as a function of AoL from  $50^\circ$  (higher HIC) to  $120^\circ$  (lower HIC) due to the differential phase delay between the two model classes. As discussed in Section 6.2, the uncertainty in phase of Neptune's strongest magnetic wave, associated with the 14-hr synodic period, also impacts the strength and orientation of the induced MMs. It also dictates the constructive or destructive interference pattern of the 14 and 141-hr total induced MMs (characterized with ionosphere HIC in the range of 0 S–30,000 S), thus setting constraints on the separability between model classes.

In addition to optimizing the altitude at closest approach and the AoL, the approach angle (i.e., latitude and longitude coverage) of the Triton flyby can have an impact on the magnitude of the scaling matrix and the associated MS between the two model classes. The baseline trajectory (T0) is approximately oriented at a  $45^\circ$  angle in the  $x$ - $y$  plane of Triton's geographical frame, optimized such that the latitude at closest approach is near  $0^\circ$  where there is the greatest chance to fly over the induced magnetic pole where the field is two times as large as it is at the magnetic equator. (This trajectory is associated with the Trident Concept Study Report, submitted to NASA in November 2020 in response to the Science Mission Directorate's Discovery 2019 Announcement of Opportunity. Trident featured a single flyby by Triton with a specific AoL of  $50^\circ$  and flyby trajectory of  $\sim 45^\circ$ , selected by the Trident team as a joint optimization among multiple science objectives.) To provide guidance for future single or multiple flyby missions, four additional hypothetical trajectories (T1–T4) were defined to explore the trajectory trade space. These hypothetical trajectories are idealized as straight paths spanning a  $\pm 6$ -min period about closest approach, and are characterized as having the same velocity (18.75 km/s) and altitude (340 km) at closest approach as the baseline trajectory. The AoL is held constant at  $50^\circ$ .

Panel (a) of Figure 13 illustrates the five trajectories T0–T4 and panels (b) and (c) represent the dipolar matrix coefficients and associated scaling matrices for the baseline (T0) and T1 trajectories, respectively. Panel (d) of the figure illustrates the MS of the least-favorable likely ocean case with the ionosphere-only models, averaged over all phases of the synodic period and plotted as a function of ionosphere HIC, achieved for all 5 trajectories. Panels (e) and (f) represent the MS between the least-favorable likely ocean case and the ionosphere models, plotted against ionosphere HIC, for 12 different magnetic phases associated with the Trajectories T0 and T1, respectively. Trajectory T1 is parallel to the  $y$ -axis and lies in Triton's equatorial plane ( $0^\circ$  latitude). While the baseline (T0) trajectory has a scaling matrix  $S_{\text{SMM}}$  with non-zero mixing coefficients (e.g.,  $M_y$  and  $M_z$  feed into  $PC_1$ ), the T1 trajectory yields a purely diagonal scaling matrix  $S_{\text{SMM}}$  where there is no mixing of MM components. Trajectory T1 is optimal because it has the largest average ocean-to-ionosphere MS for all ionosphere HIC, due to the relatively large coefficients in the diagonal scaling matrix ( $S_{11}$ ,  $S_{22}$ , and  $S_{33}$ ).

Trajectory T3, which is perpendicular to the Triton equatorial plane, results in very similar performance as T1, indicating that the proposed ocean detection methodology works best when a spacecraft flies through the point in space where T3 and T1 intersect. This occurs because the induced magnetic pole rotates in a plane roughly

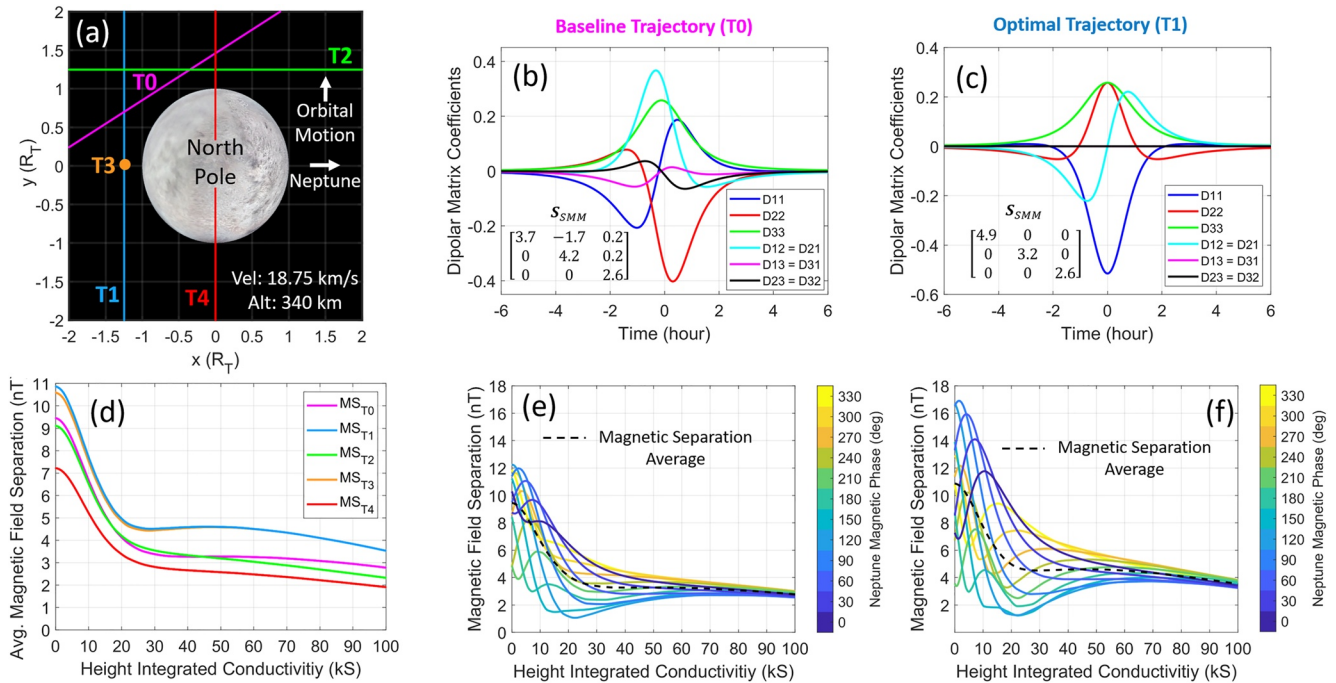


**Figure 13.** Magnetic separation of ocean-to-ionosphere PCs is influenced by the trajectory. (a) Comparison of 5 different flyby trajectory geometries. Note that T3 is perpendicular to the 2D image and comes out of the page. T1 and T2 are located in Triton's equatorial plane. T0 has a slight dependence on  $z$ , but CA is at zero latitude. T4 has a Triton latitude of  $90^\circ$  and CA is over the North Pole. (b, c) Dipolar matrix coefficients as a function of time for the baseline trajectory (T0) and optimal trajectory (T1), respectively. (d) Magnetic separation averaged across all magnetic phases of Neptune's 14-hr synodic wave as a function of ionosphere HIC for the 5 different trajectories illustrated in (a). (e, f) Ocean-to-ionosphere magnetic separation of the least-favorable likely oceans as a function of ionosphere HIC for various phases of Neptune's 14-hr synodic wave for the baseline trajectory (T0) and optimal trajectory (T1), respectively.

defined by the geographic equator of Triton where the induced dipolar field is stronger. For the same reason, the T4 trajectory flying over the geographic pole has minimal MS as the induced magnetic pole is never oriented in this direction, no matter the magnetic phase of Neptune.

## 6.2. Sensitivity to Unknown Phase of 14-hr Wave

The phase of Neptune's 14-hr magnetic wave will be unknown prior to the arrival of a future spacecraft. Thus, new measurements will be required in Neptune's magnetosphere to update the existing field model to accurately account for magnetic phase in the spherical harmonic coefficients. This phase uncertainty has implications on the total MMs for a single encounter based on the constructive and destructive interference with the 141-hr orbital magnetic wave. Any proposed Triton ocean-detection methodology must account for the unknown 14-hr magnetic phase at arrival in the Neptune system. The method described in this article has been extensively analyzed to assure confident ocean detection for any 14-hr magnetic wave phase possibility. To simulate a different magnetic phase  $\varphi$  with respect to the existing magnetic field model of Neptune for a given instance in time, the spherical harmonic coefficients are modified by:

$$\tilde{g}_n^m = g_n^m \cos(m\varphi) - h_n^m \sin(m\varphi), \quad (23)$$

$$\tilde{h}_n^m = h_n^m \cos(m\varphi) + g_n^m \sin(m\varphi), \quad (24)$$

and the magnetic field is recomputed using Equation 1 with the modified coefficients.

As the 14-hr magnetic phase varies from  $0^\circ$  to  $360^\circ$ , the MMs and SMM ocean classification spaces, derived from Equation 17, also rotate by  $360^\circ$  (primarily in  $M_x$  and  $M_y$ ) where the lowest intensity ionosphere-only model is located at the origin (i.e., no magnetic induction response). Within this  $360^\circ$  rotation range, the location of the ionosphere only models with respect to the ocean-plus-ionosphere can vary, appearing to cross over and intersect in a 2-dimensional space, thus reducing the MS for certain phases of the synodic wave, but still maintaining model class isolation

when viewed in the third dimension. This reduction in MS occurs when the phase of the synodic wave is roughly in the range from  $90^\circ$  to  $180^\circ$  (noting phase is relative to the Connerney et al., 1991 magnetic field model). Because the PCA eigenvectors align the data along the PCs of greatest variance, the classification space does not perfectly rotate as the MMs or SMMs for different phases of the synodic period. This is illustrated in panels (a)–(f) of Figure 16 where the 14-hr magnetic phase has been varied in increments of  $60^\circ$ . The associated MS between model class achieved by PCA is plotted as a function of ionosphere HIC in panels (g)–(l) of Figure 16. The worst-case scenario occurs when the phase of the 14-hr wave is near  $120^\circ$  and when the ionosphere HIC is in the range of 15 kS to 25 kS. Although it appears that some of the ionosphere-only models overlap with the ocean-plus-ionosphere models, the third dimension ( $PC_3$  not shown) provides enough MS to fully isolate the two classes of data (green circles) by at least 1-nT.

To improve separability, if required for such a worst-case scenario (e.g.,  $120^\circ$  magnetic phase), the 14-hr wave's dipole magnetic field contribution to the time-series can be mathematically removed from the forward modeled data. More specifically, the PC classification space is recomputed with a modified set of data defined by  $\mathbf{B}_{\text{Ind}}(t) - \mathbf{B}_{\text{Ind},14\text{RM}}(t)$ , where the latter term represents the dipolar magnetic field time-series associated with the 14-hr wave for a single selected reference model (RM) with the associated MM:

$$\mathbf{M}_{14\text{RM}}(t) = -A_{14\text{RM}} e^{-i\phi_{14\text{RM}}} \mathbf{B}_{N,14\text{RM}}(t), \quad (25)$$

where the  $A_{14\text{RM}}$  is the amplitude and  $\phi_{14\text{RM}}$  is the phase delay of the selected RM. Note that use of a single RM does not—and need not—completely remove the 14-hr dipolar field contribution exactly for all models. Instead, it transforms the PC space into one that effectively provides a partially removed 14-hr wave, which is shown to still be adequate. Once the actual measurement is acquired, prior to projection into the altered PC space using the updated eigenvectors, the dipolar magnetic field time-series associated with the 14-hr wave reference  $\mathbf{B}_{\text{Ind},14\text{M}}(t)$  is removed from the noisy measurement. Because the same RM is removed from the forward modeled data and the measurement, no error is introduced by this process. Note also that this model subtraction method would only rarely be necessary; specifically, only when all the following conditions are met: (a) a hard-to-detect ocean (thin and with low-conductivity) is present, (b) ionosphere HIC is in the range 15–25 kS, and (c) Neptune's magnetic phase happens to be near  $120^\circ$  with respect to the Connerney et al. (1991) field model. When the ionosphere HIC is greater than 30 kS, the 14-hr wave becomes less influential, as it does not have the ability to penetrate the highly conducting ionosphere; the MS is minimally affected by the variation of phase of this wave. As will be demonstrated in the next section, this subtraction technique would not be required in a multi-pass mission, as PCA can combine the measurement data sets from each encounter for improved MS.

### 6.3. Multiple Encounters

Although the discussion so far has been limited to applicability of the method for a single flyby, the PCA ocean detection (and characterization) approach is not restricted to a single encounter and can easily be adapted for a multi-flyby orbiter mission. PCA affords additional advantages to multi-pass orbiter missions, beyond that delivered for a single flyby, when multi-sets of magnetic induction fields are concatenated into a single input matrix. The PCA ocean detection methodology allows data from a series of passes or flybys to be concatenated into a single design matrix, similar to how the magnetometer channels were concatenated for a single flyby. As an example, panel (a)–(b) of Figure 14 illustrates five separate hypothetical trajectories associated with five different positions of Triton along its inclined orbit (AoL =  $+90^\circ$ ,  $+45^\circ$ ,  $0^\circ$ ,  $-45^\circ$ ,  $-90^\circ$ ). Panel (c) of Figure 14 illustrates the associated MS for the least-favorable likely ocean cases (50 km ocean thickness and 9 S/m conductivity), beginning with AoL of  $+90^\circ$ , for one-, two-, three-, four-, and five-flyby scenarios.

When magnetic field data sets from multiple trajectories are concatenated and used as input into PCA, the eigenvectors expand from a vector length of  $3-6N$  for two flybys, to  $9N$  for three flybys, and so on. New information is contained within the data acquired from these additional flybys, including variation in trajectory angle with respect to the direction of Neptune (change in dipolar matrix), the trajectory velocity that impacts the number of samples used for processing, and the change in MMs associated with the variation in the driving magnetic fields. PCA maximizes the variance in this larger data set, thereby resulting in a set of eigenvectors (3 by  $15N$  in the case for 5 flybys) that yield a set of new PCs. The additional information presented to the algorithm results in improved MS compared to that achieved from a single flyby mission as it maximizes that data variance across all passes. As a result, the method has the ability to tighten constraints for ocean characterization as described in Section 9.

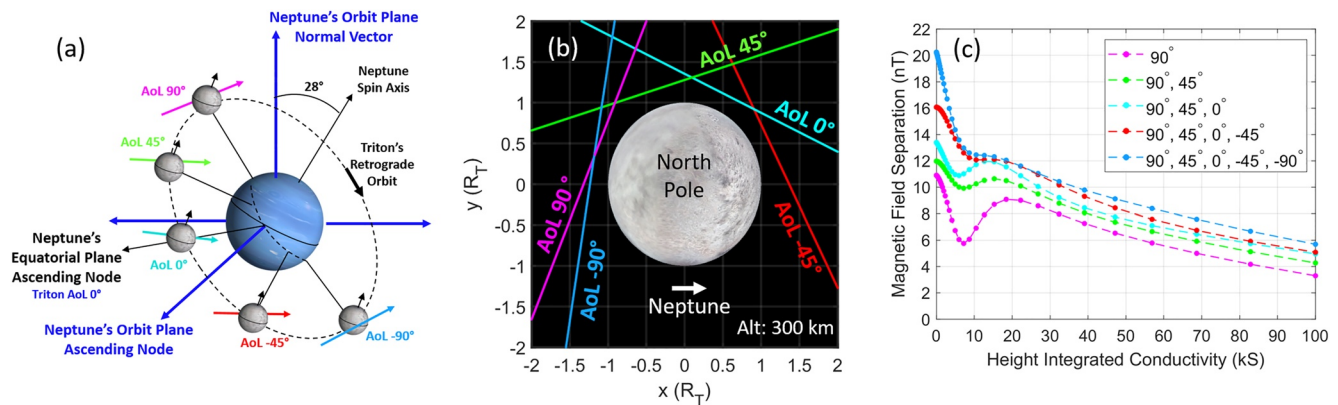


**Figure 14.** Magnetic separation, and hence classification margin, can be improved with added encounters. (a–b) Comparison of 5 different available single-pass trajectories (developed under Trident) corresponding to times when Triton is at AoL of  $+90^\circ$ ,  $+45^\circ$ ,  $0^\circ$ ,  $-45^\circ$ ,  $-90^\circ$  and (c) the corresponding least-favorable likely ocean-to-ionosphere magnetic separation as a function of ionosphere HIC for one- (starting with AoL of  $90^\circ$ ), two-, three-, four-, and five-flyby scenarios.

## 7. Sensitivity to Noise and Error Sources

### 7.1. Sensitivity to Loss of Data

PCA also affords additional flexibility of ocean detection in the event of various forms of data loss. One such example is when measurement data for one or even two of the magnetometer channels may be lost, corrupted, or intentionally dropped due to large magnetic field perturbations generated by the moon's plasma interaction. While this would reduce ocean-to-ionosphere MS, there is no constraint that all three magnetometer channels must be used to form the design matrix  $X$  (Equation 18b). Panel (a) of Figure 15 illustrates, for the baseline trajectory T0, the sensitivity of MS for the least-favorable bounding ocean case when various magnetometer channels are dropped. Figure 15 demonstrates that ocean detection is still possible as long as  $B_x$  and/or  $B_y$  is retained. The  $B_z$  component contains very little information and is not well suited for ocean detection alone. The PCA-based approach also demonstrates robustness against unintentional full channel outages and resiliency against temporary data loss. Panels (b) and (c) of Figure 15 illustrate the effect on MS for 0.5, 1, 2, and 3-min data dropouts in all three magnetometer channels, centered around closest approach. Flexibility is also provided to selectively drop small windows of data at closest approach if the measurement is subsequently found to contain higher order moment induction signatures (e.g., from an asymmetric ocean or ionosphere) near the surface not included in the forward modeling.

### 7.2. Sensitivity to Random and Structural Noise

A Monte Carlo simulation involving all of the ionosphere-only models (51 models) and the associated least-favorable likely ocean cases (51 models) was performed to demonstrate the robustness of the methodology when

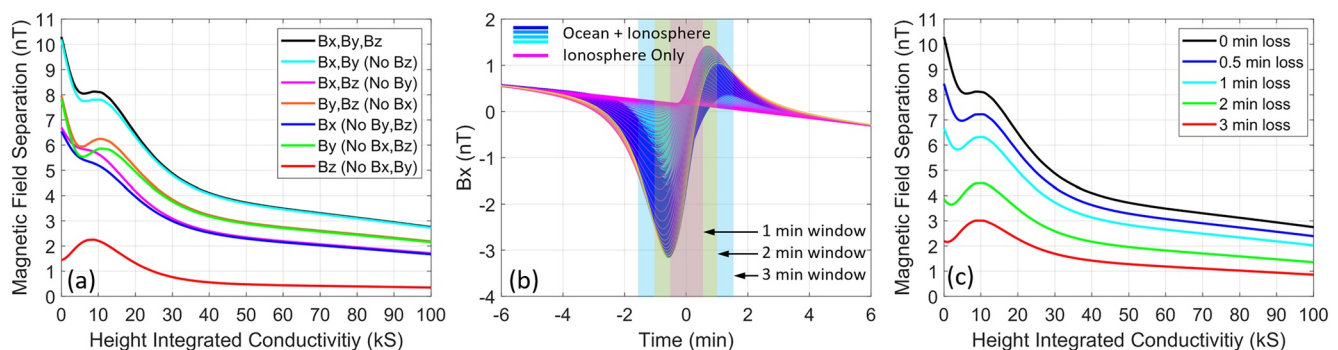


**Figure 15.** PCA is robust to various forms of data loss. (a) Comparison of the ocean-to-ionosphere magnetic separation for the least-favorable likely ocean as a function of ionosphere HIC resulting from different combinations of the three magnetometer channels being used by PCA. (b) Illustration depicting different windows of data loss in all channels (only  $B_x$  channel shown) and (c) the ocean-to-ionosphere magnetic separation for the least-favorable likely ocean as a function of ionosphere HIC for each of the data loss cases illustrated in (b).

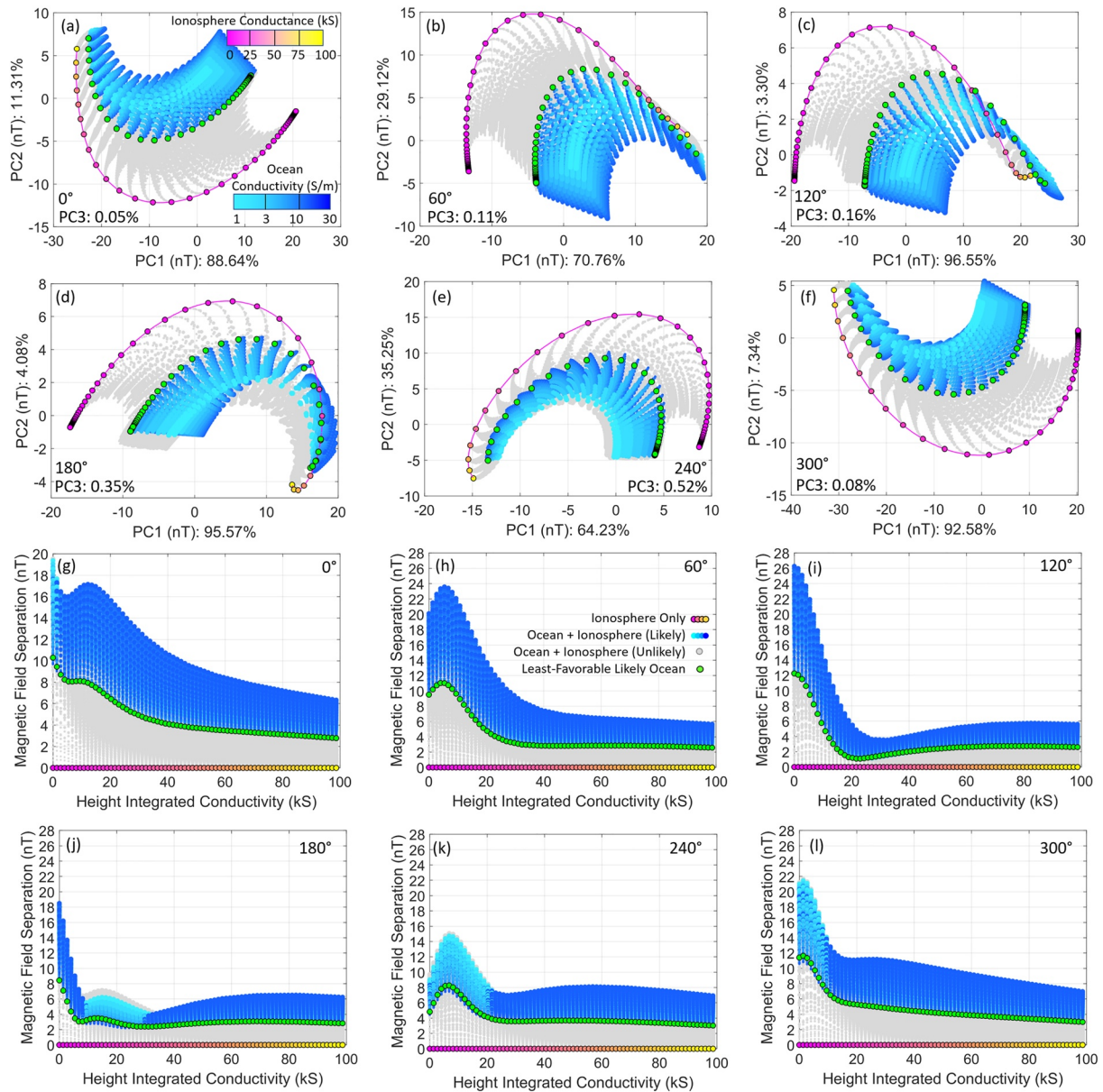


**Figure 16.** Magnetic separation of ocean-to-ionosphere models depends on the phase of Neptune's synodic wave, which will be unknown prior to arrival. Panels (a–f) comparison of the PC space (2 of 3 dimensions shown) for various magnetic phases of Neptune at increments of  $60^\circ$  relative to the  $0^\circ$  Connerney et al. (1991) model baseline. Note that the majority of the variance is explained by PC1 and PC2 as indicated by the labels of each axis; however, there is a third principal axis (not shown in these plots) that in this analysis is very important, as it is useful in separating the ocean and ionosphere models, which appear to overlap for magnetic phases in the range from  $90^\circ$  to  $180^\circ$ . Panels (g–l) Ocean-to-ionosphere magnetic separation plots versus ionosphere HIC for the 3-dimensional PC spaces illustrated in panels (a–f). Note that for the most likely oceans (those ocean cases above the green-colored models), complete separability is achieved between all ionosphere models. The best-case Neptune magnetic phase for ionosphere HIC in the range of 0–10 kS corresponds to  $120^\circ$ , coincidentally the worst-case magnetic separation for ionosphere HIC is in the range of 20 to 30 kS. In this latter HIC region, the least-favorable likely ocean case, represented by the green circles, is separated from the ionosphere models by 1 nT, which is sufficient as dictated by the noise analysis presented in Section 7.2.

faced with various patterns of noise. A set of 1,000 simulated flybys with different noise characteristics was simulated for each of the 102 models, assuming a magnetic phase of  $0^\circ$ . The instrument noise model used was based on the performance of a fluxgate magnetometer having an electronics white noise of 30 pT and sensor flicker noise characterized with 30 pT at 1-Hz and 300 pT at 1-mHz.

The spacecraft error sources (held constant for each of the 1,000 flybys) include a  $1^\circ$  ( $3\sigma$ ) attitude uncertainty in each axis, 1 ( $3\sigma$ ) second timing error, and 10 km ( $3\sigma$ ) position uncertainty in each dimension. A DC offset error

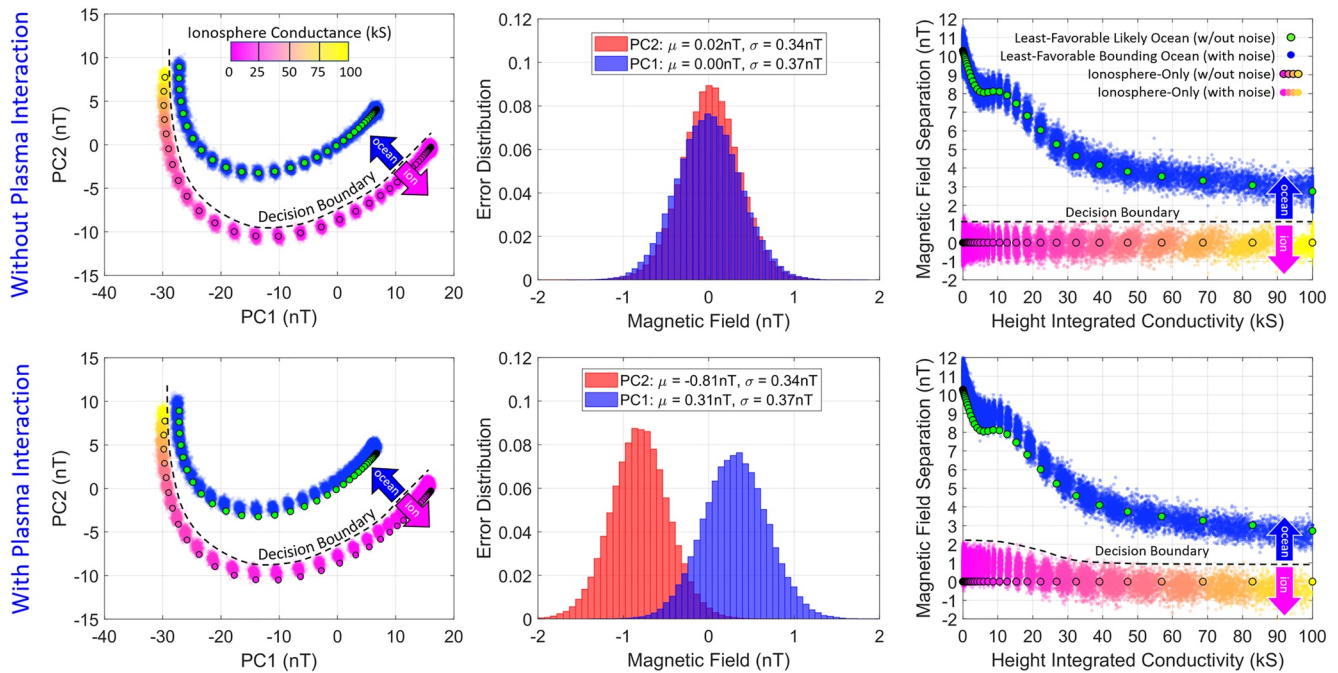


**Figure 17.** The proposed method is robust to various noise sources. Monte Carlo simulation results are shown with various sources of noise described in the text (top row) without and (bottom row) with plasma interaction fields present. The left two panels represent the PC space for both simulations, the middle panels represent the absolute PC position error (for largest two components) extracted from the simulated measurements, and the right panels illustrate the separation distance of the models, projected into a 2-dimensional space as a function of ionosphere HIC.

was also introduced into the measurements (also held constant) with 0.1 nT ( $3\sigma$ ) uncertainty, representing the *residual offset* residing in each axis after in-flight calibration retrieval of the undistinguishable stray spacecraft fields, fluxgate sensor offsets, and electronics offsets. A deviation in the complex response function (amplitude and phase delay) by 1% ( $3\sigma$ ) for each magnetic wave at the various frequencies in the simulated measurements was included in the analysis to account for modeling unknowns.

Coincidentally for the trajectory used for this article, the magnetic phase of  $0^\circ$  established in the baseline Connerney et al. (1991) model corresponds to a spacecraft time-of-arrival when Triton is crossing Neptune's magnetic equator, where plasma density is anticipated to be at a maximum. To ensure PCA's robustness against plasma interaction fields, the plasma density of the current sheet assumes 10 times the density of what Voyager encountered. However, hybrid modeling described in Liuzzo et al. (2021) reveals that the plasma interaction fields are relatively small for the baseline trajectory when Triton is at an AoL of  $50^\circ$  (see Figure 5) due to the favorable magnetic field-plasma flow angle. Even at other AoLs, the maximum magnetic field perturbations generated by the plasma interaction are only on the order of 1 nT (see Figures 4 and 6 in Liuzzo et al., 2021); however, these occur when Triton is many Neptune radii away from the plasma sheet where the plasma densities are expected to be much lower than those simulated. Thus, for the purposes of this analysis, there is no need to remove the modeled plasma interaction field effects from the magnetic field measurements. Instead, the plasma effects are absorbed as a tolerable structured noise source. Table A2 in the Appendix provides a more detailed summary of the noise and error sources included in this analysis.

After simulating 1,000 flybys for each of the ionosphere-only and ocean-plus-ionosphere models, PCA is used to project the noisy data into the PC classification space as defined in Equation 20. Figure 17 illustrates the results of the PC space, PC error distribution, and PC ionosphere-to-ocean separation distance of the Monte Carlo simulations with inclusion of the various noise sources. The top three panels are associated with the simulation that does not include the plasma-induced effects and the bottom panels include them. As illustrated in the PC space for both cases, the noise alters the absolute position of a model in the PC space depending on the ionosphere intensity (here shown in two dimensions). In the plasma-free case, each simulated measurement is projected into the classification space within a *noise sphere* with  $3\sigma$  radius of roughly 1 nT, corresponding to the PC error distributions (middle panels). Positive ocean detection occurs if the PCA projected measurement falls on the ocean side of the decision boundary defined in the figure as the line that bounds the noisy ionosphere-only models.

When the plasma-induced fields are included, the simulated measurements also are projected into a region defined by a 1 nT noise sphere. However, in this case, the plasma interaction fields have the effect of offsetting the sphere's position. Here, the models have their PC1 shifted by 0.31 nT and their PC2 shifted by 0.81 nT. Because the offsets for each axis are different and the ocean decision boundary shares multiple dimensions, the boundary is modified and takes on an ionospheric HIC dependence as illustrated in the bottom right plot of Figure 17. Note that the relative separation between all ocean models and their corresponding ionospheres is preserved, but their absolute position is not. Because of this, the decision boundary is raised to 2 nT (with respect to the noise-free ionosphere models for ionospheres characterized with HIC <20 kS), but the 1 nT level boundary for ionosphere HIC greater than 20 kS is maintained to ensure proper classification when plasma effects are not assumed to be present. Note that the reduction of MS between ocean and no-ocean models with ionosphere HIC <20 kS is not a concern, as there is already large separation due to the impact of the stronger 14-hr wave. As mentioned above, plasma-induced fields are treated as a noise source in this analysis. No attempt is made to model and remove their impact, as their presence is tolerable to the method, especially when the low probability of the plasma current sheet being sufficiently close to Triton is considered. However, if by chance the plasma-induced currents happen to be unexpectedly larger than anticipated, they can be modeled (see Liuzzo et al., 2021) and then partially removed prior to classification.

## 8. Detectable Oceans for a Single-Pass Trajectory

For a single flyby mission, the confidence in the detection of a potential sub-surface ocean increases with increased MS of the model classes in the ocean classification space. For a given ionosphere HIC and 14-hr magnetic phase, MS varies as a function of the ocean model's physical attributes. The thickness of the ice shell strongly influences the MS because of the  $1/r^3$  dipole falloff associated with the ocean's depth below Triton's surface. Oceans with less conductivity also have a smaller induction response to Neptune's driving magnetic waves. Figure 18 illustrates the ocean-to-ionosphere MS contours as a function of ocean thickness and ocean conductivity for 12 different scenarios corresponding to different combinations of Neptune's 14-hr magnetic phase and ionosphere HIC. Note that only models with ocean conductivity of 10 S/m or less are shown for clarity. Superimposed on each of the 12 panels is a black dashed contour region highlighting the most likely ocean cases, consistent with Figure 6.

From the noise analysis results in Section 7, it was determined that any ocean-plus-ionosphere model that is spaced within 1-nT of an ionosphere-only model is indistinguishable from another and therefore cannot be positively labeled as an ocean with certainty. In Figure 18, this indistinguishable region is represented by the red contour and represents the ocean models that cannot definitely be detected. The worst-case MS of the data set shown occurs when the magnetic phase is  $120^\circ$  and the ionosphere HIC is 30 kS. In this case, all of the most likely ocean models (contained within the dashed line) are detectable with at least 2-nT of MS from the ionosphere-only model. Note that for each of the data sets with ionosphere HIC of 50 kS and above, the contours for any given magnetic phase of the synodic period look similar, as this wave is attenuated by the high ionospheric conductance and therefore plays less of a role in magnetic induction within the ocean. This data set indicates that even for a single encounter using the baseline trajectory; a large ocean parameter space can be uniquely differentiated from an ionosphere response, even in the presence of various sources of noise and a highly conducting ionosphere.

## 9. Ocean and Ionosphere Characterization for a Multi-Pass Trajectory

The method described in this article is not only able to distinguish the induction response of an ocean-plus-ionosphere from that of an ionosphere-only response, but it can also characterize the interior profile based on where the projected measurement lands in the 3-dimensional classification space. The spatial location of the projection provides an estimate of the ocean conductivity and thickness as well as the ionosphere conductance. The panels of Figure 19 illustrate characterization contours associated with three representative oceans for a single flyby (column 1), three flybys (column 2), and five flybys (column 3), for four different ionosphere HIC values (rows). The contour boundaries, owing to three different levels of noise (1, 0.5, and 0.1 nT), encompass the ocean models that are indistinguishable from the underlying ocean. The assumed noise dictates the uncertainty of model parameters, thereby setting constraints on characterization of the ocean thickness and conductivity. As illustrated, the ocean thickness and conductivity of a putative subsurface ocean at Triton can be broadly constrained for a single flyby. However, as more flybys are added, ocean-to-ionosphere and ocean-to-ocean model separation distances increase (See Section 6.3), hence tightening the precision of the estimated parameters of the underlying oceans.

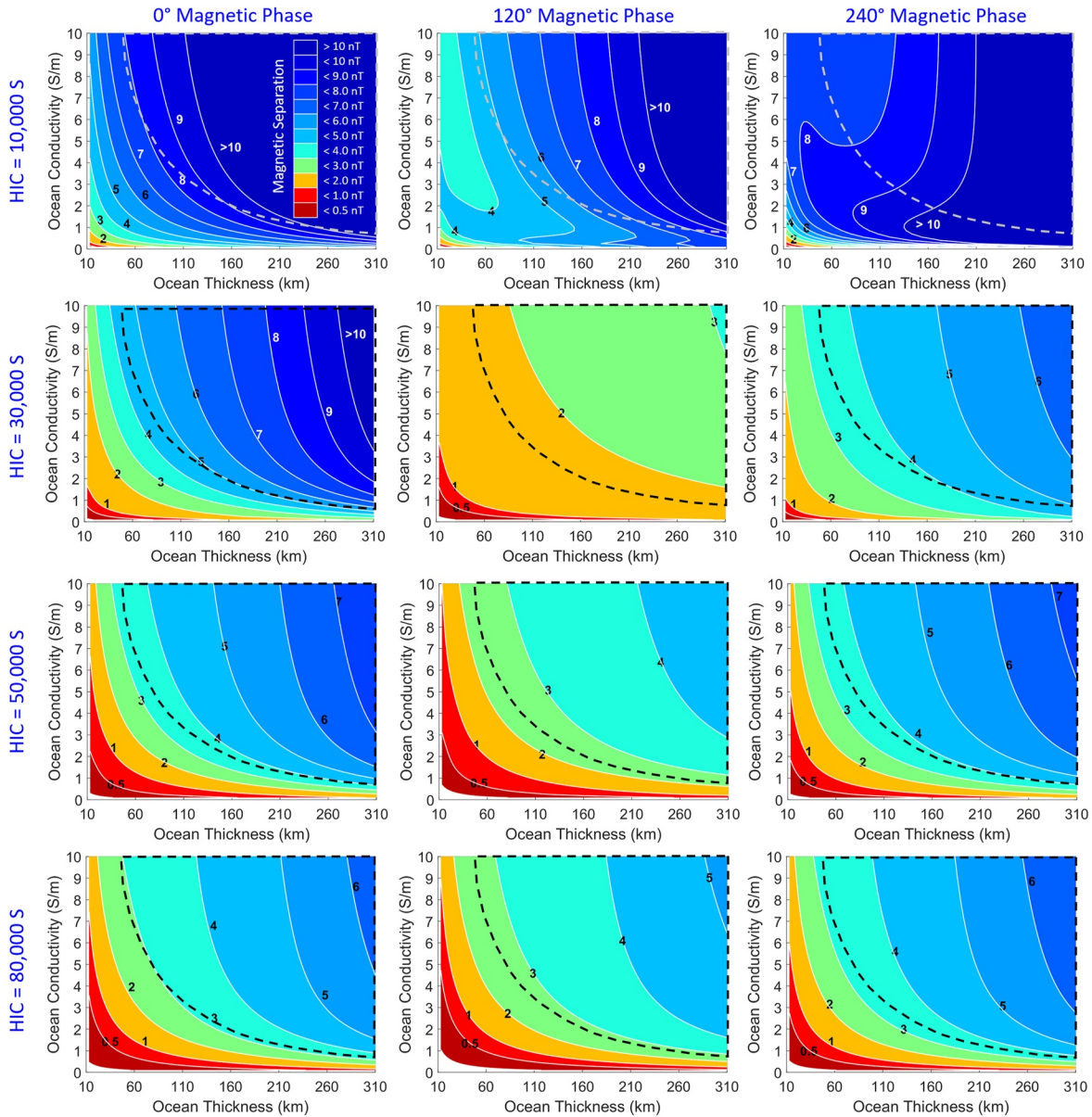


**Figure 18.** Dependence of ocean-to-ionosphere magnetic separation for range of ionosphere HIC and Neptune magnetic phase for a single-flyby. Each panel represents the magnetic separation contours (units of nT) of the ocean-plus-ionosphere models from the ionosphere-only models as a function of ocean thickness and ocean conductivity for (left column) magnetic phase of 0°, (middle column) worst-case magnetic phase of 120°, and (right column) 240°, for ionosphere HIC of 10, 30, 50, and 80 kS. Black dashed region highlights the most likely ocean space (§2.3). The red contours indicate magnetic separation below 1nT, where ocean classification or differentiation could not be performed with certainty.

As the ocean thickness decreases and the surface depth increases, ocean conductivity becomes more difficult to discern. Estimates of ocean conductivities and ocean thicknesses improve with multiple flybys across the entire ionosphere intensity range, including HIC levels above 50,000 S where the 14-hr wave has less ability to penetrate the ionosphere and contribute to induction.

## 10. Conclusions

Increasing scientific interest in ocean worlds highlights the need for advances in analytic techniques to positively determine the presence of subsurface oceans in challenging environments. The PCA based analysis method described in this article represents a new paradigm for processing space-based magnetometer measurements, with demonstrated advantages in reliably distinguishing the presence and key characteristics of a conductive

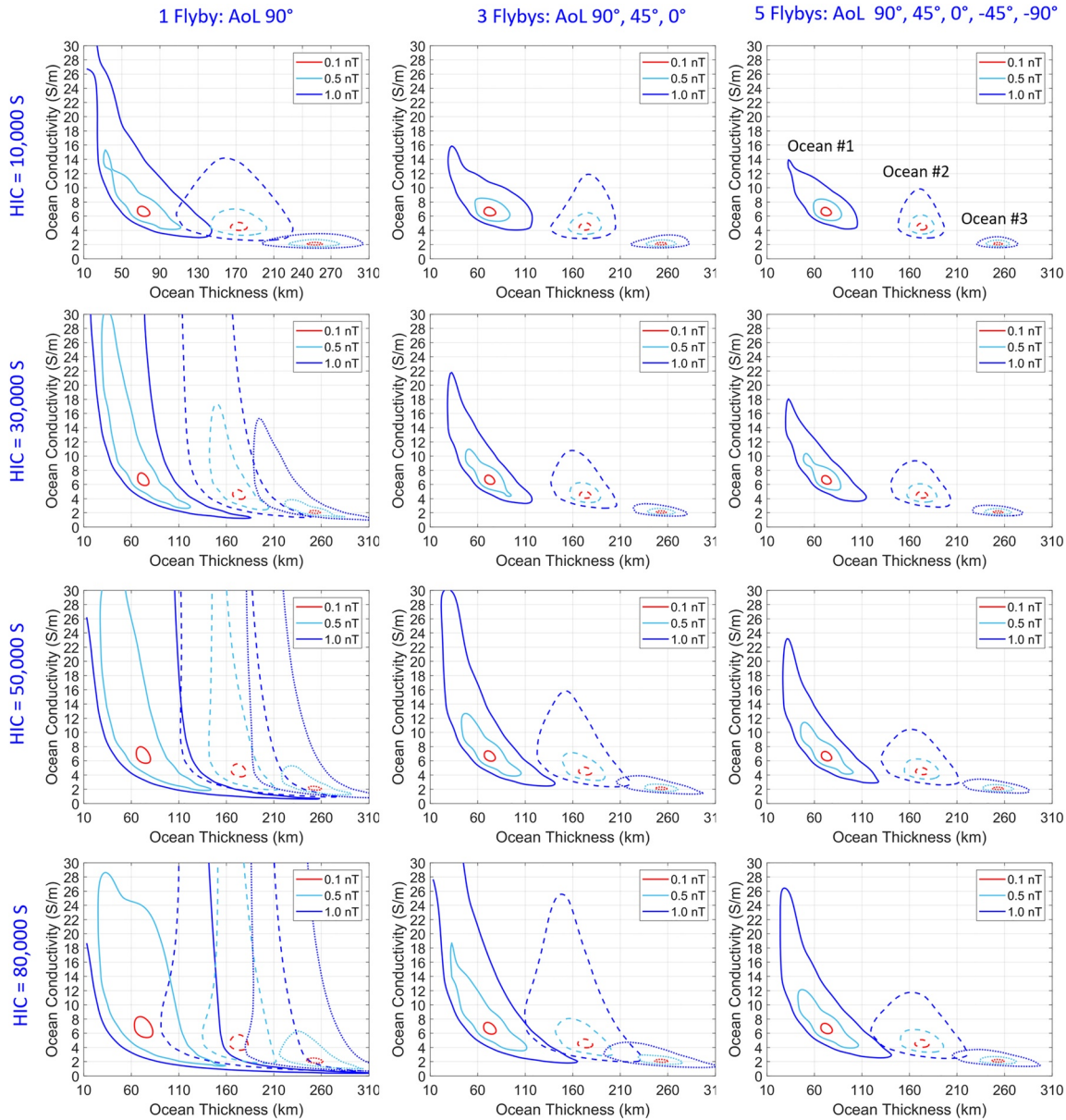


**Figure 19.** Measurements from multiple flybys can be used to improve confidence in the estimation of ocean parameters. Each panel in the figure illustrates characterization contours of three representative oceans for (left column) one flyby at AoL of  $+90^\circ$ , (middle column) three flybys at AoL of  $+90^\circ$ ,  $+45^\circ$  and  $0^\circ$  and (right column) five flybys at AoL of  $+90^\circ$ ,  $+45^\circ$ ,  $0^\circ$ ,  $-45^\circ$ , and  $-90^\circ$ , where each row corresponds to a different ionosphere HIC scenario. Ocean #1 ( $T_o = 75$  km,  $\sigma = 6.5$  S/m) is represented by the solid lines, ocean #2 ( $T_o = 175$  km,  $\sigma = 4.5$  S/m) is represented by the dashed lines, and ocean #3 ( $T_o = 255$  km,  $\sigma = 2.0$  S/m) is represented by the dotted lines. The three contours shown for each ocean represent the boundaries that encompasses the indistinguishable oceans when three different levels of noise are considered (blue = 1 nT, cyan = 0.5 nT, and red = 0.1 nT).

liquid layer even in the face of the confounding factors of a conductive ionosphere, local plasma interaction currents, systemic uncertainties, and various noise and error sources. Unique features of the PCA method provide additional advantages of flexibility and resiliency. MS between the ocean-plus-ionosphere and ionosphere-only model classes is maintained even with incomplete input data, while flexibility to pre-select measurement data channels or data time intervals enables selective removal of contaminated data if necessary. Using Neptune's largest moon Triton as an example ocean world, PCA was directly applied to a three-axis magnetic induction field data set and shown to be a powerful ocean classification tool, distinguishing the induced magnetic responses of ionosphere-only cases from those of the ionospheres convolved with candidate potential oceans, even on a single flyby. The flexibility and extensibility afforded by the PCA-based method enhance the existing and future capabilities for ocean detection and characterization at candidate ocean worlds throughout the solar system.

Appendix

**Table A1**  
*List of the Frequencies and Amplitudes of the Magnetic Waves Encountered by Triton*

Label	Frequency ( $\mu\text{Hz}$ )	Period (hr)	$B_x$ (nT)	$B_y$ (nT)	$B_z$ (nT)
DC	0	-	0.2057	0.009	-3.0633
$f_s$	19.2125	14.4582	6.7834	3.4094	0.3759
$f_o$	1.9694	141.0457	2.574	1.2847	0.189
$2f_s$	38.4250	7.2291	0.2563	0.1713	0.0092
$3f_s$	57.6375	4.8194	0.0042	0.0032	0.0001
$2f_o$	3.9388	70.5229	0.0593	0.0394	0.0067
$f_s - f_o$	17.2431	16.1095	0.2481	0.0122	1.3562
$f_s + f_o$	21.1819	13.1139	0.2568	0.1714	0.0088
$f_s - 2f_o$	15.2737	18.1867	0.2697	0.1362	0.0513
$f_s + 2f_o$	23.1513	11.9983	0.0041	0.003	0.0002
$f_s - 3f_o$	13.3043	20.8789	0.0107	0.0069	0.0008
$f_s + 3f_o$	25.1208	11.0577	0.0002	0	0
$2f_s - f_o$	36.4556	7.6196	0.0085	0.0022	0.0687
$2f_s + f_o$	40.3944	6.8766	0.009	0.0068	0.0002
$2f_s - 2f_o$	34.4862	8.0548	0.0205	0.001	0.0027
$2f_s + 2f_o$	42.3638	6.5570	0.0002	0.0001	0.0001

Note.  $f_s$  represents the synodic frequency and  $f_o$  represents the orbital frequency.

**Table A2**  
*List of the Error Sources Included in the Monte Carlo Simulation*

Measurement error source	Error parameter	Error value
Spacecraft ephemeris uncertainty	Attitude uncertainty (all axes)	$\pm 1^\circ$ ( $3\sigma$ )
	Timing uncertainty	$\pm 1$ s ( $3\sigma$ )
	Position uncertainty (all axes)	$\pm 10$ km ( $3\sigma$ )
Instrument noise	Electronics white noise	30 nT
	Sensor flicker noise	30 nT @ 1 Hz
		300 nT @ 1 mHz
Deviation in complex response function	Amplitude deviation (all frequencies)	$\pm 1\%$ ( $3\sigma$ )
	Phase deviation (all frequencies)	$\pm 1\%$ ( $3\sigma$ )
DC level (residual after offset calibration)	Spacecraft field, sensor offset	$\pm 0.1$ nT ( $3\sigma$ )
Plasma interaction fields	Plasma density	Electrons: 0.03–0.11 $\text{cm}^{-3}$
		Ions: 0.03–0.11 $\text{cm}^{-3}$
	Plasma temperature	30 eV electrons
		65 eV ions
	Plasma composition	50% N+/50% H+
		$\langle m \rangle > 7.5$ amu
	Plasma speed (relative to Triton)	43 km/s
Local magnetic field strength	Alfven speed	125–200 km/s
	N <sup>+</sup> gyroradius at Triton	5–8 nT
		598–1,315 km

Note. Plasma interaction fields details are described further in Liuzzo et al. (2021).

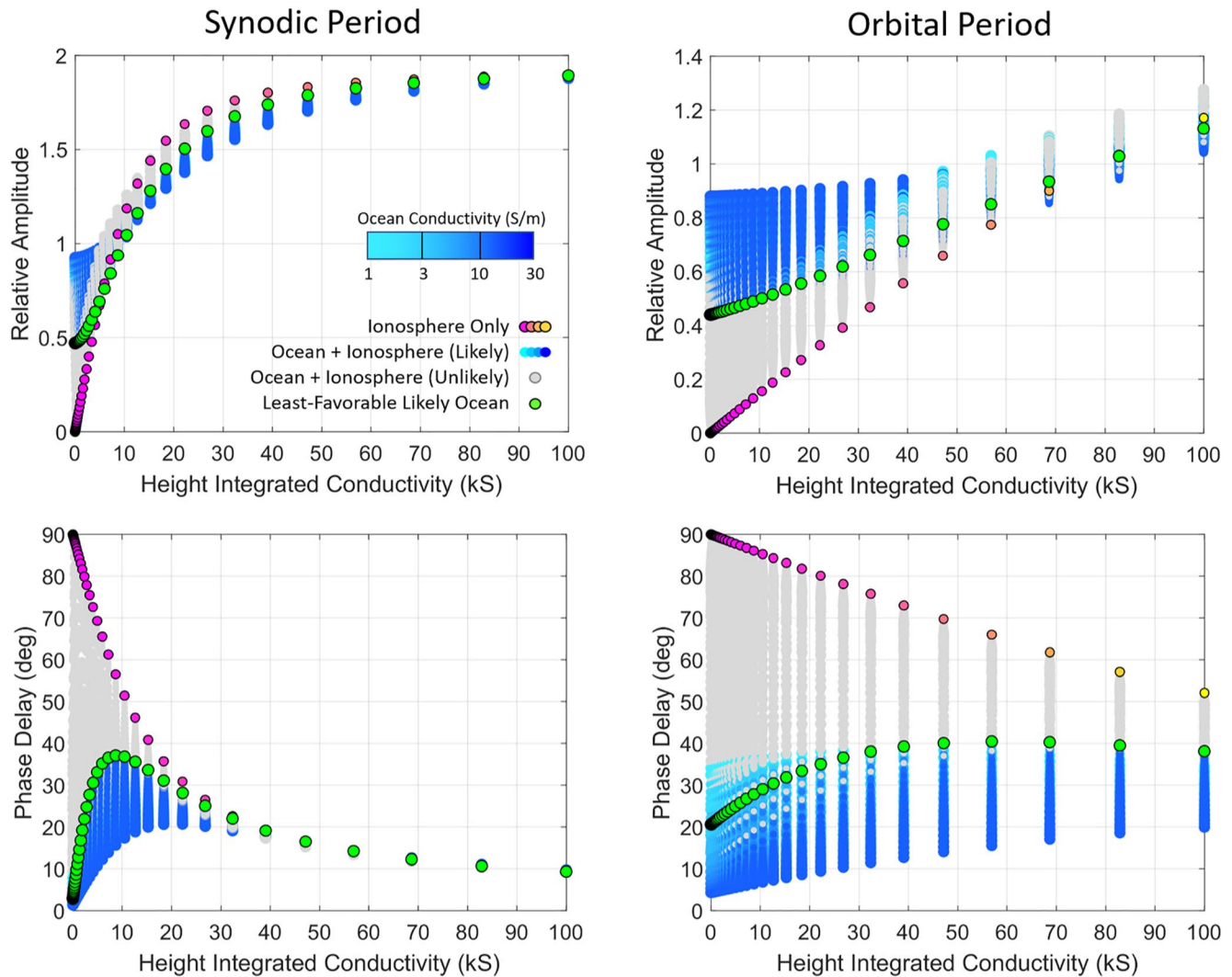


**Figure A1.** Relative amplitude and phase delay of the ionosphere-only and ocean-plus-ionosphere models used in this analysis, plotted as a function of ionosphere HIC for both the (left panels) 14-hr synodic and the (right panels) 141-hr orbital periods. Note that although the discriminability between the ionosphere-only models and the least-favorable likely ocean models in the amplitude response of the orbital wave is low and almost non-existent for the amplitude response of the synodic wave, the phase delay, especially at the 141-hr period, provides the differences in response needed to facilitate robust classification between the two model classes for the full range of ionosphere HICs used in the study.

### Data Availability Statement

The data contained in this publication are archived on Zenodo at [doi.org/10.5281/zenodo.5484442](https://doi.org/10.5281/zenodo.5484442). The data are stored in Matlab .mat structure files with an associated .m script for easy data extraction. For all timing and ephemeris computation in this work, the NAIF developed SPICE toolkit for Matlab called mice ([https://naif.jpl.nasa.gov/naif/toolkit\\_MATLAB.html](https://naif.jpl.nasa.gov/naif/toolkit_MATLAB.html)) was utilized. All magnetic field models and field line visuals were implemented in MATLAB. The most recent kernel files (pck00010.tpc, naif0012.tls, de435.bsp, de431.tpc, nep081.bsp, nep095.bsp) were leveraged and all IAU defined reference frames defined in the IAU working group report (Archinal et al., 2018) were used.

### References

- Alken, P., Maute, A., Richmond, A., Vanhamäki, H., & Egbert, G. (2017). An application of principal component analysis to the interpretation of ionospheric current systems. *Journal of Geophysical Research: Space Physics*, 122, 5687–5708. <https://doi.org/10.1002/2017ja024051>
- Archinal, B. A., Acton, C. H., Hearn, M. F. A., Conrad, A., Consolmagno, G. J., Duxbury, T., et al. (2018). Report of the IAU working group on cartographic coordinates and rotational elements: 2015. *Celestial Mechanics and Dynamical Astronomy*, 130, 22. <https://doi.org/10.1007/s10569-017-9805-5>

### Acknowledgments

The authors thank Krishan Khurana of UCLA for fruitful discussions on magnetic induction and plasma interaction at Triton, Michael Turmon of JPL for his insights into the PCA ocean detection approach and Try Lam of JPL for the design of the trajectories used in this work. The research was carried out at the Jet Propulsion Laboratory, California Institute of Technology, under a contract with the National Aeronautics and Space Administration (80NM0018D0004). Funding support was provided by the NASA Discovery Program, as part of the Trident mission Phase A study (80NM0020F0034).

- Arridge, C. S., Eggington, J. W. B. (2021). Electromagnetic induction in the icy satellites of Uranus. *Icarus*, *367*, 114562. <https://doi.org/10.1016/j.icarus.2021.114562>
- Castillo-Rogez, J., Daswani, M. M., Glein, C., Vance, S., Cochrane, C. J. (2021). Contribution of non-water ices to salinity and electrical conductivity in ocean worlds. *Role of non-water ices in driving ocean salinity and electrical conductivity in ocean worlds*. <https://doi.org/10.1002/essoar.10509076.1>
- Cochrane, C. J., Vance, S., Nordheim, T., Styczinski, M. J., Masters, A., Regoli, L. H. (2021). In search of subsurface oceans within the Moons of Uranus. *JGR Planets*, *126*(12), e2021JE006956. <https://doi.org/10.1029/2021JE006956>
- Comnerney, J., Acuna, M. H., & Ness, N. F. (1991). The magnetic field of Neptune. *Journal of Geophysical Research*, *96*, 19023–19042. <https://doi.org/10.1029/91ja01165>
- Croft, S., Kargel, J., Kirk, R. L., Moore, J., Schenk, P., & Strom, R. (1995). The geology of Triton. In *Neptune and Triton* (pp. 879–947).
- Croft, S. K., & Soderblom, L. A. (1991). In J. T. Bergstrahl (Ed.), *Geology of the Uranian satellites*. Uranus (pp. 561–628). Tucson, AZ: University of Arizona Press.
- Eckhardt, D. H. (1963). Geomagnetic induction in a concentrically stratified Earth. *Journal of Geophysical Research*, *68*, 6273–6278. <https://doi.org/10.1029/jz068i023p06273>
- Hannachi, A., Jolliffe, I., & Stephenson, D. (2007). Empirical orthogonal functions and related techniques in atmospheric science: A review. *International Journal of Climatology*, *27*, 1119–1152. <https://doi.org/10.1002/joc.1499>
- Hansen, C. J., Castillo-Rogez, J., Grundy, W., Hofgartner, J. D., Martin, E. S., Mitchell, K., et al. (2021). Triton: Fascinating Moon, likely ocean world, compelling destination!. *The Planetary Science Journal*, *2*, 137. <https://doi.org/10.3847/psj/abffid>
- Hartkorn, O., & Saur, J. (2017). Induction signals from Callisto's ionosphere and their implications on a possible subsurface ocean. *Journal of Geophysical Research: Space Physics*, *122*(11), 11–677. <https://doi.org/10.1002/2017ja024269>
- Hendrix, A. R., Hurford, T. A., Barge, L. M., Bland, M. T., Bowman, J. S., Brinckerhoff, W., et al. (2019). The NASA Roadmap to ocean worlds. *Astrobiology*, *19*, 1–27. <https://doi.org/10.1089/ast.2018.1955>
- Hubbard, W. B., Podolak, M., & Stevenson, D. J. (1995). Interior of Neptune. In D. Cruickshank (Ed.), *Neptune and Triton* (pp. 109–138). Tucson: University of Arizona Press.
- Ip, W. H. (1990). On the ionosphere of Triton: An evaluation of the magnetospheric electron precipitation and photoionization effects. *Geophysical Research Letters*, *17*, 1713–1716. <https://doi.org/10.1029/g1017i010p01713>
- Ivanov, M., & Borozdin, V. (1991). Enigmatic circular features in the Cantaloupe terrain on Triton. In *Lunar and planetary science conference*.
- Jolliffe, I. T., & Cadima, J. (2016). Principal component analysis: A review and recent developments. *Philosophical Transactions of the Royal Society A: Mathematical, Physical and Engineering Sciences*, *374*, 20150202. <https://doi.org/10.1098/rsta.2015.0202>
- Khurana, K. K., Kivelson, M. G., Stevenson, D. J., Schubert, G., Russell, C. T., Walker, R. J., & Polansky, C. (1998). Induced magnetic fields as evidence for subsurface oceans in Europa and Callisto. *Nature*, *395*(6704), 777–780. <https://doi.org/10.1038/27394>
- Kirk, R. L., Soderblom, L. A., Brown, R., Kieffer, S., & Kargel, J. (1995). Triton's plumes: Discovery, characteristics, and models. In *Neptune and Triton* (pp. 949–989).
- Kivelson, M. G., Khurana, K. K., Stevenson, D. J., Bennett, L., Joy, S., Russell, C. T., et al. (1999). Europa and Callisto: Induced or intrinsic fields in a periodically varying plasma environment. *Journal of Geophysical Research A*, *104*, 4609–4625. <https://doi.org/10.1029/1998JA900095>
- Kivelson, M. G., Khurana, K. K., & Volwerk, M. (2002). The permanent and inductive magnetic moments of Ganymede. *Icarus*, *157*, 507–522. <https://doi.org/10.1006/icar.2002.6834>
- Lamy, L. (2020). Auroral emissions from Uranus and Neptune. *Philosophical Transactions of the Royal Society A: Mathematical, Physical and Engineering Sciences*, *378*(2187). <https://doi.org/10.1098/rsta.2019.0481>
- Liuzzo, L., Paty, C., Cochrane, C., Nordheim, T., Luspay-Kuti, A., Castillo-Rogez, J., et al. (2021). Triton's variable interaction with Neptune's magnetospheric plasma. *Journal of Geophysical Research: Space Physics*, *126*, e2021JA029740. <https://doi.org/10.1029/2021ja029740>
- Liuzzo, L., Simon, S., & Feyerabend, M. (2018). Observability of Callisto's inductive signature during the JUPITER ICy moons Explorer mission. *Journal of Geophysical Research: Space Physics*, *123*(11), 9045–9054. <https://doi.org/10.1029/2018ja025951>
- Liuzzo, L., Simon, S., Feyerabend, M., & Motschmann, U. (2016). Disentangling plasma interaction and induction signatures at Callisto: The Galileo C10 flyby. *Journal of Geophysical Research: Space Physics*, *121*(9), 8677–8694. <https://doi.org/10.1002/2016ja023236>
- Liuzzo, L., Simon, S., Feyerabend, M., & Motschmann, U. (2017). Magnetic signatures of plasma interaction and induction at Callisto: The Galileo C21, C22, C23, and C30 flybys. *Journal of Geophysical Research: Space Physics*, *122*(7), 7364–7386. <https://doi.org/10.1002/2017ja024303>
- Mandt, K. E., & Luspay-Kuti, A. (2019). Comparative planetology of the ion chemistry and Pluto, Titan, and Triton. *Pluto System After New Horizons*, *LPI Contributions*, 2133.
- Mejnertsen, L., Eastwood, J. P., Chittenden, J. P., & Masters, A. (2016). Global MHD simulations of Neptune's magnetosphere. *Journal of Geophysical Research: Space Physics*, *121*(8), 7497–7513. <https://doi.org/10.1002/2015ja022272>
- Müller, J., Simon, S., Motschmann, U., Schüle, J., Glassmeier, K. H., & Pringle, G. J. (2011). AIKEF: Adaptive hybrid model for space plasma simulations. *Computer Physics Communications*, *182*(4), 946–966.
- Nimmo, F., & Pappalardo, R. T. (2016). Ocean worlds in the outer solar system. *Journal of Geophysical Research: Planets*, *121*(8), 1378–1399. <https://doi.org/10.1002/2016JE005081>
- Nimmo, F., & Spencer, J. R. (2015). Powering Triton's recent geological activity by obliquity tides: Implications for Pluto geology. *Icarus*, *246*, 2–10. <https://doi.org/10.1016/j.icarus.2014.01.044>
- Nimmo, F., Spencer, J. R., Pappalardo, R. T., & Mullen, M. E. (2007). Shear heating as the origin of the plumes and heat flux on Enceladus. *Nature*, *447*, 289–291. <https://doi.org/10.1038/nature05783>
- Podolak, M., Weizman, A., & Marley, M. (1995). Comparative models of Uranus and Neptune. *Planet. Planetary and Space Science*, *43*(12), 1517–1522. [https://doi.org/10.1016/0032-0633\(95\)00061-5](https://doi.org/10.1016/0032-0633(95)00061-5)
- Porco, C. C., Helfenstein, P., Thomas, P. C., Ingersoll, A. P., Wisdom, J., West, R., et al. (2006). Cassini observes the active South Pole of Enceladus. *Science*, *311*(5766), 1393–1401. <https://doi.org/10.1126/science.1123013>
- Rebello, L. R. R., Siepman, T., & Drexler, S. (2020). Correlations between TDS and electrical conductivity for high-salinity formation brines characteristic of South Atlantic pre-salt basins. *WaterSA*, *46*, 602–609. <https://doi.org/10.17159/wsa/2020.v46.i4.9073>
- Ruzmaikin, A. A., & Starchenko, S. V. (1991). On the origin of Uranus and Neptune magnetic fields. *Icarus*, *93*, 82–87. [https://doi.org/10.1016/0019-1035\(91\)90165-p](https://doi.org/10.1016/0019-1035(91)90165-p)
- Saur, J., Duling, S., Roth, L., Jia, X., Strobel, D. F., Feldman, P. D., et al. (2015). The search for a subsurface ocean in Ganymede with Hubble Space Telescope observations of its auroral ovals. *JGR Space Physics*, *120*(3), 1715–1737. <https://doi.org/10.1002/2014JA020778>
- Saur, J., Neubauer, F. M., & Glassmeier, K. H. (2010). Induced magnetic fields in solar system bodies. *Space Science Reviews*, *152*(1), 391–421. <https://doi.org/10.1007/s11214-009-9581-y>

- Schenk, P. M., Moore, J. M., & Schenk, P. M. (2020). Topography and geology of Uranian mid-sized icy satellites in comparison with Saturnian and Plutonian satellites. *Philosophical Transactions of the Royal Society A: Mathematical, Physical, and Engineering Sciences*, 378, 20200102. <https://doi.org/10.1098/rsta.2020.0102>
- Schilling, N., Khurana, K. K., & Kivelson, M. G. (2004). Limits on an intrinsic dipole moment in Europa. *Journal of Geophysical Research*, 109, E05006. <https://doi.org/10.1029/2003JE002166>
- Sittler, E., & Hartle, R. (1996). Triton's ionospheric source: Electron precipitation or photoionization. *Journal of Geophysical Research: Space Physics*, 101, 10863–10876. <https://doi.org/10.1029/96ja00398>
- Soderlund, K. M., & Stanley, S. (2020). The underexplored frontier of ice giant dynamos. *Philosophical Transactions of the Royal Society A: Mathematical, Physical, and Engineering Sciences*, 378(2187). <https://doi.org/10.1098/rsta.2019.0479>
- Stanley, S., & Bloxham, J. (2004). Convective-region geometry as the cause of Uranus' and Neptune's unusual magnetic field. *Nature*, 428, 151–153. <https://doi.org/10.1038/nature02376>
- Stanley, S., & Bloxham, J. (2006). Numerical dynamo models of Uranus' and Neptune's magnetic fields. *Icarus*, 184(2), 556–572. <https://doi.org/10.1016/j.icarus.2006.05.005>
- Strobel, D. F., Simmers, M. E., Herbert, F., & Sandel, B. R. (1990). The photochemistry of methane in the atmosphere of Triton. *Geophysical Research Letters*, 17, 1729–1732. <https://doi.org/10.1029/g1017i010p01729>
- Tyler, G., Sweetnam, D., Anderson, J., Borutzki, S., Campbell, J., Eshleman, V., et al. (1989). Voyager radio science observations of Neptune and Triton. *Science*, 246, 1466–1473. <https://doi.org/10.1126/science.246.4936.1466>
- Vance, S. D., Styczinski, M. J., Bills, B. G., Cochrane, C. J., Soderlund, K. M., Gómez-Pérez, N., & Paty, C. (2021). Magnetic induction responses of Jupiter's ocean moons including effects from adiabatic convection. *Journal of Geophysical Research: Planets*, 126, e2020JE006418. <https://doi.org/10.1029/2020JE006418>
- Weiss, B. P., Biersteker, J. B., Colicci, V., Goode, A., Castillo-Rogez, J. C., Petropoulos, A. E., & Balint, T. S. (2021). Searching for subsurface oceans on the moons of Uranus using magnetic induction. *Geophysical Research Letters*, 48, e2021GL094758. <https://doi.org/10.1029/2021GL094758>
- Yung, Y., & Lyons, J. (1990). Triton: Topside ionosphere and nitrogen escape. *Geophysical Research Letters*, 17, 1717–1720. <https://doi.org/10.1029/g1017i010p01717>
- Zhang, M., Richardson, J. D., & Sittler, E. C., Jr. (1991). Voyager 2 electron observations in the magnetosphere of Neptune. *Journal of Geophysical Research*, 96(S01), 19085–19100. <https://doi.org/10.1029/91ja01857>
- Zimmer, C., Khurana, K. K., & Kivelson, M. G. (2000). Subsurface Oceans on Europa and Callisto: Constraints from Galileo magnetometer observations. *Icarus*, 147, 329–347. <https://doi.org/10.1006/icar.2000.6456>